J. Fluid Mech. (2002), *vol.* 470, *pp.* 31–61.
DOI: 10.1017/S002211200200839X Printed in the United Kingdom

The manipulation of the streamwise vortex instability in a natural convection boundary layer along a heated inclined flat plate

By MARK A. TRAUTMAN[1] AND ARI GLEZER[2]

[1]Intel Corporation, Hillsboro, OR 97124, USA

[2]The George W. Woodruff School of Mechanical Engineering, Georgia Institute of Technology, Atlanta, GA 30332, USA

(Received 20 December 1999 and in revised form 14 December 2001)

Flow instabilities leading to the formation of streamwise vortices in a natural convection boundary layer over a heated inclined plate submerged in a water tank are manipulated using spanwise arrays of surface-mounted heating elements. The flow over the plate is driven by a two-ply surface heater comprised of a uniform, constant-heat flux heater and a mosaic of 32×12 individually controlled heating elements that are used as control actuators. Surface temperature distributions are measured using liquid crystal thermography and the fluid velocity in cross-stream planes is measured using particle image velocimetry (PIV). Time-invariant spanwise-periodic excitation over a range of spanwise wavelengths leads to the formation of arrays of counter-rotating streamwise vortex pairs and to substantial modification of the surface temperature and heat transfer. The increase in surface heat transfer is accompanied by increased entrainment of ambient fluid and, as a consequence, higher streamwise flowrate. Subsequent spanwise-periodic merging of groups of vortices farther downstream retards the streamwise increase of the surface heat transfer rate. Finally, the suppression of small-amplitude spanwise disturbances by linear cancellation is demonstrated.

1. Introduction

The amplification of three-dimensional instabilities within a natural convection boundary layer over an inclined heated flat plate can lead to the formation of streamwise (longitudinal) vortices having a mean spanwise spacing that decreases with increasing surface heat flux (Shaukatullah & Gebhart 1978). The three-dimensional motions that are induced by the appearance of these vortices lead to an increase in the surface heat transfer of the base flow, thus suggesting that controlled manipulation of these vortices can result in further enhancement of the surface heat transfer. In the present work, the formation and evolution of streamwise vortices that are triggered by excitation of the flow instabilities that lead to their formation are investigated with particular emphasis on changes in the surface heat transfer.

The appearance of streamwise vortices in an inclined natural convection boundary layer was first reported by Sparrow & Husar (1969) who used a thymol-blue technique for flow visualization. They conjectured that a streamwise instability of these vortices is the first stage of transition to turbulence for plate inclination angles that are greater than 15°. Flow visualization also revealed that the characteristic spanwise wavelength

of the vortices decreases with increasing surface temperature and is only weakly dependent on the inclination angle of the plate, and that neighbouring vortices merge prior to breakdown to turbulence. In a later investigation, Lloyd & Sparrow (1970) showed that depending on the inclination angle, the plate boundary layer becomes unstable in two modes: two-dimensional ($\theta < 14^\circ$, transverse travelling waves) or three-dimensional ($\theta > 17^\circ$, leading to the formation of steady longitudinal vortices). The critical Rayleigh number for the onset of these instabilities decreases from 10^9 for $\theta = 0^\circ$ to 10^6 at $\theta = 60^\circ$.

The temperature and velocity along an inclined heated plate operated at constant heat flux was measured in detail by Shaukatullah & Gebhart (1978) who also presented an extensive literature survey of other experimental, analytical and numerical work in this area. They observed that for inclination angles exceeding 11°, the appearance of travelling waves is preceded by streamwise vortices. Similar to a heated plate operated at constant surface temperature, the wavelength of the spanwise instability is independent of the inclination angle, and inversely proportional to the surface heat flux. The onset of the instability depends on the modified Grashof number ($G^* = 5(\frac{1}{5}Gr^*)^{1/5}$, where Gr^* is the Grashof number based on surface heat flux) and the streamwise distance from the leading edge. This dependence on streamwise position was lumped into a dimensionless transition measure for the onset of the streamwise vortex instability (originally proposed by Jaluria & Gebhart 1974) $E = R(v^2/gx^3)^{2/15}$ or $E = 88\theta^{-0.65}$. The onset and evolution of the instability modes of the base flow can be substantially modified by exploiting their receptivity to controlled external disturbances leading to substantial modifications of the base flow. This approach was first employed by Schubauer & Skramstad (1948) who used a vibrating ribbon to explore the evolution of two-dimensional waves in a flat-plate isothermal (momentum) boundary layer. The growth rates and propagation velocities of the imposed disturbances compared well with the theoretical predictions of Schlichting (1933). Klebanoff, Tidstrom & Sargent (1961) used a vibrating ribbon with spanwise variations to introduce controlled three-dimensional wave disturbances into the two-dimensional base flow in order to study their nonlinear evolution and the onset of transition to turbulence. In a similar experiment in a natural convection boundary layer, Jaluria & Gebhart (1973) also used a spanwise non-uniform vibrating ribbon to investigate the nonlinear evolution of controlled time-periodic disturbances. Passive forcing using strips of tape adhered to the surface was used by Zuercher, Jacobs & Chen (1998) to investigate the onset and merging of streamwise vortices in a natural convection boundary layer along an inclined isothermal surface. These experiments showed that the breakdown of the vortices occurred at a fixed transition Reynolds number, which was larger than predicted by the nonlinear stability analysis of Chen *et al.* (1991). Nevertheless, it is noteworthy that the ratio of the Reynolds numbers of vortex onset and breakdown predicted by the experiments and the analyses are similar. Details of other experimental and analytical investigations are reviewed in the works of Zuercher *et al.* (1998) and Chen *et al.* (1991).†

The present investigation focuses on the coupling between the fluid mechanics and heat transport within a buoyancy-driven boundary layer over a constant heat flux surface with specific emphasis on the evolution of actively forced spatial disturbances and the subsequent formation and merging of spanwise-regular streamwise vortices

† After the review of the present paper was completed, we became aware of the recent work of Jeschke & Beer (2001) who investigated the evolution of unforced longitudinal vortices and their effect on the heat transfer in a natural convection boundary layer over an inclined heated flat plate.

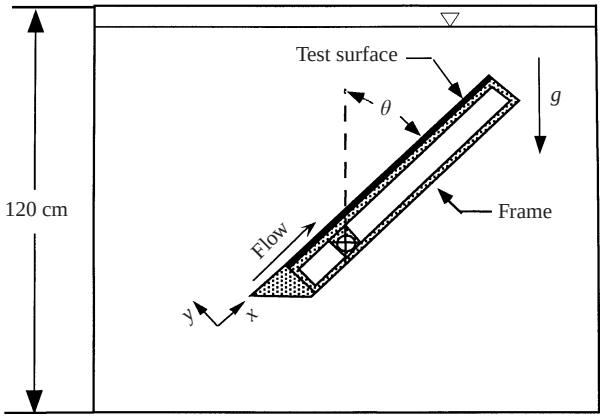

FIGURE 1. Diagram of the test facility.

(Trautman 1999). Of particular interest are the resulting modification of the base flow and the characterization of the concomitant heat transport from the surface. Section 2 describes the experimental hardware including the water facility, the test surface, surface actuators, and the procedures and instrumentation that were used to measure the surface temperature and the fluid velocities. The unforced base flow is characterized in § 3. The effects of the forcing including the formation and merging of the streamwise vortices are discussed in § 4.

2. Experimental apparatus and diagnostics

The experiments are conducted in a water tank using a heated submerged flat test surface, as shown schematically in figure 1. Flow instabilities leading to the formation of streamwise vortices are manipulated using a mosaic of surface heating actuators mounted on a ceramic substrate 66 cm long and 61 cm wide. The width of the surface is approximately 50 wavelengths of the nominal spanwise instability that leads to the formation of streamwise vortices. The ceramic substrate is mounted on a stainless steel frame, hinged along its span to a support rod that is attached the sidewalls of the tank, and the inclination angle of the test surface is adjusted using a mechanical hoist. An external circulation system is used to either cool or heat the water in the tank to the desired temperature.

Zuercher *et al.* (1998) considered the sensitivity of the flow to three leading-edge configurations and the majority of their data was taken on a surface that had a 5.08 cm long unheated starting length. The leading edge of the plate that is used in the present experiments has a sharp wedge-like leading edge with a 16° undercut at the tip (figure 1) and, similar to the plate of Zuercher *et al.* (1998), has a 5.08 cm long unheated section upstream of the heated test section.

2.1. *The heated test surface*

The test surface is comprised of a two-layer Kapton insulated foil heater bonded to a ceramic plate with thermal conductivity of $0.42\ \mathrm{W\,m^{-1}\,K^{-1}}$. The top layer is a uniform 12.7 μm thick Inconel foil heater connected to an electrode along each of its spanwise edges. The bottom layer is a mosaic of individually controlled heating elements (figure 2) comprised of three identical segments each 20 cm wide and 56 cm long in the streamwise (x) direction. Each segment includes 32 copper–nickel film elements (40 Ω

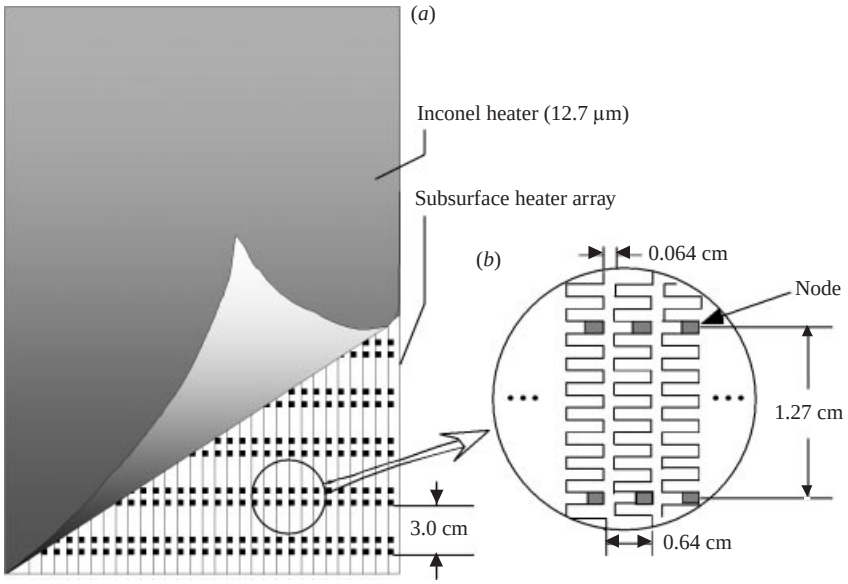

FIGURE 2. (*a*) The two-ply heater surface. (*b*) Enlarged view of the individual heating elements and their node connections (the array has 384 nodes).

each) serpentined in the streamwise direction (figure 2*b*). The individual elements are 0.64 cm wide × 56 cm long, and the centre-to-centre distance between adjacent elements is 0.64 cm. The electrical leads to the actuator nodes are connected within an air cavity beneath the ceramic substrate such that each actuator segment can be externally wired to achieve a desired spatial forcing pattern. The actuators are driven by a bank of 32 amplifiers that can be controlled directly from the laboratory computer.

The discrete heating elements induce spanwise temperature gradients on the surface which produce streamwise vorticity Ω_x. This is readily evident by considering the streamwise (x) component of the time invariant vorticity equation at the wall ($y = 0$). For a given inclination angle, the magnitude and sign of the time-averaged production of streamwise vorticity at the wall ($g\beta \sin(\theta)\partial T_s/\partial z = v\partial^2\Omega_x/\partial^2 y$) depends on the spanwise surface temperature gradient (neglecting viscosity temperature sensitivity), and, consequently, by imposing a specific spanwise temperature gradient along the surface, positive and negative streamwise vorticity can be introduced into the flow. The spanwise temperature gradient also produces a normal component of vorticity at the surface ($g\beta \cos(\theta)\partial T_s/\partial z = -v\partial^2\Omega_y/\partial^2 y$) which becomes more important as the plate inclination angle decreases.

Because the energy in the natural convection boundary layer increases downstream owing to the continuous streamwise heating at the surface, an actuator operating at a fixed power becomes less effective when it is located downstream. Therefore, a dimensionless forcing amplitude Q_r having a spanwise-periodic forcing wavelength λ is defined as the ratio of the actuator power relative to the power input by the uniform heater up to the streamwise location of the actuators, or

$$Q_r = \frac{\int_z^{z+\lambda} q_a'' L_a \mathrm{d}z}{\int_z^{z+\lambda} q_s'' L_{ea} \mathrm{d}z},$$

where q''_a and L_a are the actuator heat flux and its streamwise length, respectively, and q''_s and L_{ea} are the uniform surface heat flux and streamwise length between the actuator and the leading edge of the surface heater, respectively. If the spanwise period of the excitation waveform is discretized by N adjacent actuators each of width W, and if all the actuators operate at the same heat flux q''_a, then the actuation heat flux over one spanwise period is:

$$q''_a(z) = q''_a(z+\lambda) = q''_o \sum_{i=0}^{N-1} [U(z - \mathrm{i}W) - U(z - (\mathrm{i}+1)W)] S_N(\mathrm{i}),$$

where $U(z)$ is a unit step function and S_N is a Boolean shape factor that indicates the state of the active actuators (i.e. $S_N(\mathrm{i}) = 0$ or 1). For example, a forcing waveform having a spanwise period discretized by three actuators (0.64 cm apart), and a Boolean shape factor $S_3 = [1, 0, 0]$, is a square wave having a wavelength $\lambda = 1.9$ cm and duty cycle $\hat{d} = 0.33$. Using this formulation, the forcing amplitude averaged over one period of the spanwise waveform is

$$Q_r = \frac{q''_o(z) L_a \hat{d}}{q''_s L_{ea}}.$$

In the present work, the power dissipated by each heating element is typically 0.87 W and $0.12 < Q_r < 0.3$ for most cases.

2.2. *Instrumentation*

2.2.1. *Liquid crystal thermometry*

Temperature distributions on the test surface are measured using liquid crystal thermometry. Three platinum RTDs mounted 20 cm apart on a vertical stand are used (in a four-wire configuration) to measure the ambient water temperature and calibrate the liquid crystal sensor. Before each calibration begins, it is verified that the time averaged (over a 5 min period) tank temperature over the entire length of the test surface is uniform to within $\pm 0.02\,^{\circ}$C. The liquid crystal sensing element is a 0.12 mm thick polyester sheet sprayed with liquid crystal paint (Farina *et al.* 1994), which is painted flat black on the back side, and laminated between two 0.2 mm clear polyester sheets. In the present experiments, the laminated liquid crystal sensor measures 20 cm × 40 cm (spanwise × streamwise) and has a useful underwater life of approximately 24 hours (depending on tank temperature). The liquid crystal sheet is attached to the test surface with a 0.05 mm thick double-sided adhesive acrylic tape.

Images of the liquid crystal sheet are acquired using a 640 × 480 element colour CCD camera and a frame grabber installed in a laboratory computer yielding a spatial resolution of approximately 0.27 mm. To minimize colour variations due to lighting and viewing angles the liquid crystal sensor is calibrated in position for each experiment. Lighting is provided by two off-centre 250 W spotlights equipped with infra-red and polarizing filters. During the calibration, the ambient water temperature is increased slowly (less than $0.04\,^{\circ}\mathrm{C\,min^{-1}}$) while 100 images of the liquid crystal sensor are captured by a PC every 12 s. The red, green and blue colour maps of the images are converted into maps of hue, saturation and intensity (only the hue map is used for temperature calibration). A new liquid crystal sheet has a temperature sensitivity of $0.01\,^{\circ}\mathrm{C\,hue^{-1}}$ ($25 < \mathrm{hue} < 120$) and a calibration error of $\pm 0.06\,^{\circ}$C (within a 95% confidence interval) over most of the hue range; however, water diffusion through the laminate degrades the performance of the liquid crystal material over time (during 24 hours of immersion, the error can increase to $\pm 0.1\,^{\circ}$C).

The temperature maps measured during each experiment are corrected for heat conduction through the 0.2 mm top polyester sheet (having a nominal thermal conductivity of 0.3 $W\,m\,K^{-1}$) where the heat flux is calculated by monitoring the power input to the surface heater. Uncertainties in the liquid crystal temperature calibration, surface heat flux uniformity, streamwise location, and the thickness of the overlaying polyester sheet produce a maximum precision error of 7% in the measured local Nusselt number. There is also a bias error in the measured Nusselt number that is introduced by the uncertainty in the magnitude of the thermal conductivity of the polyester sheet. However, comparisons of the present heat transfer rates with measurements of previous investigators and predictions based on two-dimensional laminar (unforced) flow indicate that the estimated thermal conductivity is reasonable. (Owing to the high spatial resolution of the liquid crystal measurements, all line-plots that show spatial variations include only every fiftieth data point.)

2.2.2. *Particle image velocimetry*

Cross-correlation based particle image velocimetry (PIV) is used to measure distributions of the streamwise and cross-stream velocity components in (x, y)-planes normal to the test surface. The particles in a given plane are illuminated by a 1 mm thick light sheet that is produced by a double-pulse Nd:YAG laser. A 1008×1016 element digital CCD camera is used to image the flow at a rate of 7.5 image pairs per second. The tank is seeded with hollow glass spheres ($\rho = 1.1\,g\,cm^{-3}$) having a nominal diameter of 11 μm. Spanwise variations of the streamwise and cross-stream velocities are mapped by traversing the laser sheet and camera in the spanwise (z) direction in 1.2 mm increments. At each spanwise location, a sequence of 50 images is acquired with the even- and odd-numbered images separated by 20 ms and consecutive even (or odd) images separated by 133 ms (the frame rate period). Images separated by 20 ms are used to compute velocity vectors in regions of relatively high velocity, whereas images separated by 133 ms are used in regions of relatively low velocity. The use of different image separation times (using the same image sequence) provides better accuracy over the entire velocity range within the boundary layer. A rectangular interrogation spot measuring 128×16 pixels (in the streamwise (x) and cross-stream (y) directions, respectively) is used to process the velocity vectors, and the image resolution is 25.6 μm $pixel^{-1}$. The worst-case uncertainty in the velocity measurements caused by the finite measurement volume (i.e. the interrogation spot size and laser sheet thickness) is about 3%. The precision error in the velocity measurement at each point is less than 2%, yielding a combined uncertainty in the velocity measurement of less than 5%. The error estimates provided for the velocity measurements do not include error sources that are associated with index of refraction gradients within the thermal boundary layer. However, the excellent agreement between measured and cross-stream velocity distributions and the analytical solutions in the two-dimensional flow regime indicate that the effects of change in the index of refraction are minimal for the present range of experimental conditions.

Particle settling on the surface of the plate during PIV measurements was unavoidable, and over the course of these experiments the surface of the plate was carefully and routinely cleaned. Before each experiment the tank was thoroughly mixed, particles were wiped off the plate, and the tank was allowed to settle for several hours. Owing to non-uniform size and density distributions, the larger and heavier particles normally settle leaving the more neutrally buoyant particles suspended in the fluid. Prior to the start of the experiment, the surface was carefully wiped with a thin sponge (to minimize fluid disturbances), and the residual motions were allowed to subside for

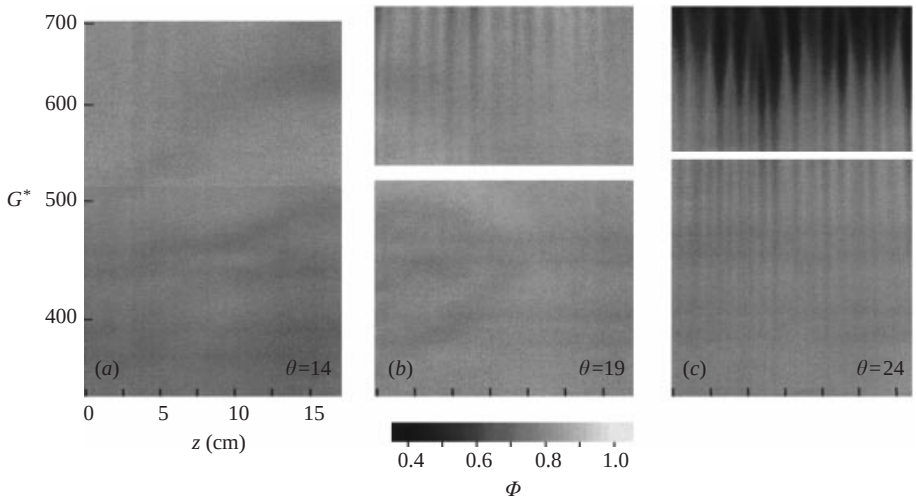

FIGURE 3. Dimensionless surface temperature maps of the unforced flow for $q'' = 2260\,\mathrm{W\,m^{-2}}$ and (*a*) $\theta = 14°$, (*b*) 19°, and (*c*) 24°.

another 30 min. After the heater was activated and the plate reached a steady heat transfer (nominally 15 min), the surface underneath the PIV interrogation domain was very slowly wiped again to minimize reflections. Following a 5 min waiting period, a 15 min measurement period was begun. The flow disturbances associated with this elaborate procedure were virtually immeasurable. (Note that no particles were seeded in the working fluid during liquid crystal measurements of the surface temperature.)

3. Velocity field and heat transfer in the unforced (baseline) flow

Distributions of the surface temperature of the unforced flow are measured within the domain $20 < x < 45\,\mathrm{cm}$ and $0 < z < 16\,\mathrm{cm}$ using liquid crystal thermography. The temperature maps at each angle are composed of two partially overlapping images each measuring 16 cm × 13 cm (spanwise × streamwise). Figures 3(*a*), 3(*b*), and 3(*c*) are grey-scale raster plots of distributions of the normalized time-averaged surface temperature $\Phi(G^*, z)$ for a surface heat flux $q'' = 2260\,\mathrm{W\,m^{-2}}$ and $\theta = 14°, 19°$ and 24°, respectively. Here, $\Phi = (T_s - T_\infty)kG^*/5xq''$, where T_s and T_∞ are the surface and ambient temperatures, k is the fluid thermal conductivity, and x is measured from the upstream edge of the uniform heater. The modified Grashof number is defined as $G^* = 5(\frac{1}{5}Gr^*)^{1/5}$ where $Gr^* = g\beta q'' x^4 \cos\theta/kv^2$ is the local Grashof number, β is the coefficient of thermal expansion, θ is the plate inclination angle (measured from vertical), and v is the kinematic viscosity. At $\theta = 14°$, Φ is almost uniform for $G^* < 690$, implying that the surface heat transfer is similar to the heat transfer in a two-dimensional laminar flow over a vertical plate since $\Phi \propto (Gr^*)^{1/5}/Nu_x$ and for two-dimensional laminar flow $Nu_x \propto (Gr^*)^{1/5}$, ($Nu_x = hx/k$ is the spanwise-averaged Nusselt number and $h = q''/(T_s - T_\infty)$ is the heat transfer coefficient). At $\theta = 19°$ (figure 3*b*), spanwise variations of Φ are first visible in the streamwise domain for $G^* > 550$. The nominally spanwise-periodic streamwise streaks (having an average spacing of 1.2 cm) are indicative of three-dimensional motions that lead to spanwise variations in the surface heat transfer. As the inclination angle increases, these variations in surface temperature intensify and are detected farther upstream.

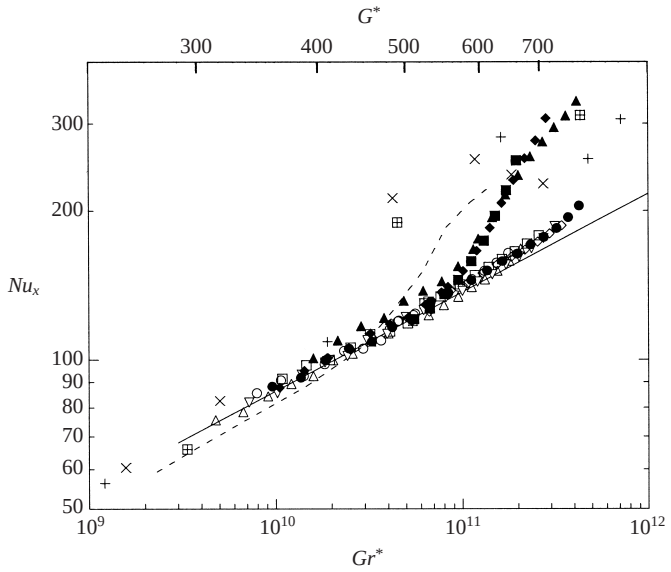

FIGURE 4. Heat transfer for the unforced flow: $\theta = 14°$: q_1'' (○), q_2'' (□), q_3'' (◇); $\theta = 19°$: q_1'' (△), q_2'' (▽), q_3'' (●); and $\theta = 24°$: q_1'' (■), q_2'' (◆), q_3'' (▲); ($q_1'' = 1380$, $q_2'' = 2260$, $q_3'' = 3800\,\mathrm{W\,m^{-2}}$). Data of Shaukatullah & Gebhart (1978) at $\theta = 29°$: $q'' = 811\,\mathrm{W\,m^{-2}}$ (×), $q'' = 2291\,\mathrm{W\,m^{-2}}$ (+), $q'' = 5049\,\mathrm{W\,m^{-2}}$ (⊞). Data of Jeschke & Beer (2001) at $\theta = 25°$, $q'' = 5269\,\mathrm{W\,m^{-2}}$ (--). The correlation $Nu_x = 0.864Gr^{*1/5}$ is shown for reference using a solid line.

At $\theta = 24°$ (figure 3*c*), the streamwise streaks begin at $G^* \approx 360$ and intensify rapidly with downstream distance resulting in a net increase in surface heat transfer relative to the two-dimensional laminar flow (as evidenced by the lower (darker) values of Φ for $G^* > 550$). The spanwise-periodic decrease in the surface temperature associated with the appearance of the streaks indicates the formation of streamwise counter-rotating vortex pairs (e.g. Sparrow & Husar 1969) that transport cooler fluid toward the surface.

Zuercher *et al.* (1998) reported spanwise meandering of the vortices prior to merging. Such meandering was also observed in the present experiments and documented in video schlieren visualization (not shown). The meandering frequency computed from these video images is estimated to be about 0.3 Hz (depending on the heat flux) and the variance of the spanwise wavelength prior to vortex merging is estimated to be about half the wavelength. In the present experiments, the sampling period of the liquid crystal measurements is sufficient to average out these spanwise fluctuations.

The temperature maps are used to compute the correlation between Nu_x and Gr^* using the spanwise-averaged local heat transfer coefficient

$$Nu_x = (x/k)\int_{z_0}^{z_1} h(x,z)\,\mathrm{d}z/(z_1 - z_0).$$

Figure 4 shows that within the streamwise domain $300 < G^* < 660$ and $\theta = 14°$ and 19° over a range of surface heat flux ($q'' = 1380$, 2260 and $3800\,\mathrm{W\,m^{-2}}$) Nu_x calculated from liquid crystal thermography measurements agrees well with the analytical solution $Nu_x = 0.864Gr^{*1/5}$ for a laminar, two-dimensional flow field. The present experiments are also in good agreement with the measurements of Shaukatullah & Gebhart (1978) for the laminar flow conditions. It is noteworthy that although streamwise streaks are clearly present at $\theta = 19°$ (figure 3*b*), the

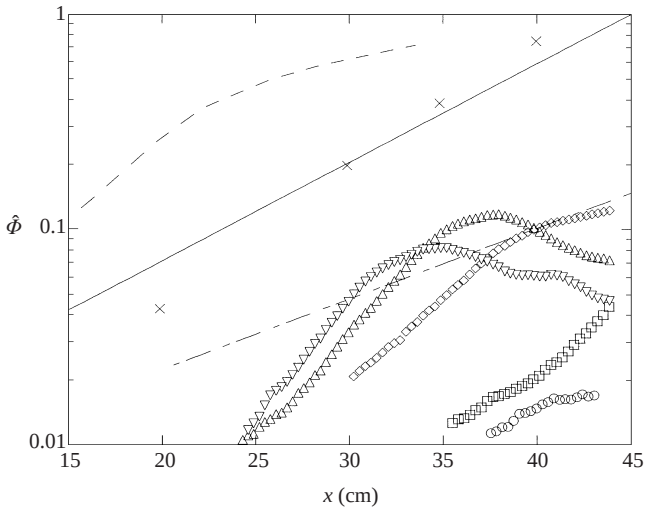

FIGURE 5. Spanwise variance of the surface temperature in the unforced flow for $q'' = 3800\,\mathrm{W\,m^{-2}}$ and $\theta = 14^\circ$ (○), 19° (□) and 24° (▽). For $\theta = 24^\circ$, data are also shown at $q'' = 1380$ (◇) and $2260\,\mathrm{W\,m^{-2}}$ (△). Data of Shaukatullah & Gebhart (1978) within the boundary layer at $y = 0.151\,\mathrm{cm}$ and $\theta = 14^\circ$, $q'' = 2250\,\mathrm{W\,m^{-2}}$ (– –), $\theta = 19^\circ$, $q'' = 2268\,\mathrm{W\,m^{-2}}$ (——), and $\theta = 29^\circ$, $q'' = 2303\,\mathrm{W\,m^{-2}}$ (-·—).

streamwise variation of the spanwise-averaged heat transfer coefficient matches the two-dimensional correlation for $G^* < 660$, implying that, in terms of heat transfer, the disturbances induced by the appearance of three-dimensional motions are relatively weak at this inclination angle and do not affect the mean flow significantly. At $\theta = 24^\circ$, however, the flow undergoes transition to three-dimensional flow around $G^* \approx 550$, where the Nu_x begins to deviate from the two-dimensional heat transfer. The data of Shaukatullah & Gebhart (1978) also show this transition, but at a lower G^* than in the present experiments (because these data were collected at a larger inclination angle $\theta = 29^\circ$). The data of Jeschke & Beer (2001) are consistent with these findings and show that for an inclination angle of $\theta = 25^\circ$, transition occurs at values of G^* that lie between the present results ($\theta = 24^\circ$) and the results of Shaukatullah & Gebhart (1978) ($\theta = 29^\circ$), ostensibly because of the difference in the inclination angles. At least within the present range of surface heat flux, the transition modified Grashof number appears to be independent of the heat flux magnitude, but relatively sensitive to the inclination angle. The deviation from the two-dimensional correlation apparently results from the appearance of streamwise flow structures that are evident in figure 3(*c*).

Streamwise amplification of the spanwise non-uniformities in the surface temperature is measured using the normalized spanwise variance $\hat{\Phi}(x) = \Phi'(x)/\bar{\Phi}(x)$ (figure 5) where $\Phi'(x)$ and $\bar{\Phi}(x)$ are the spanwise r.m.s. and spanwise-averaged levels of $\Phi(x, z)$, respectively. These data show that in the present experiments (i.e. for all inclination angles and surface heat flux levels) the initial growth of the spanwise non-uniformities is exponential with x, increases with θ, and is apparently only weakly dependent on the surface heat flux. Similar trends were observed in the boundary-layer temperature measurements of Shaukatullah & Gebhart (1978). At an inclination angle of 24°, the streamwise amplification becomes nonlinear, followed by saturation that begins farther downstream (e.g. at $x = 44$ ($G^* = 730$), 38 ($G^* = 650$), and 34 cm ($G^* = 600$) for $q'' = 1380$, 2260 and $3800\,\mathrm{W\,m^{-2}}$, respectively). Furthermore, within the present

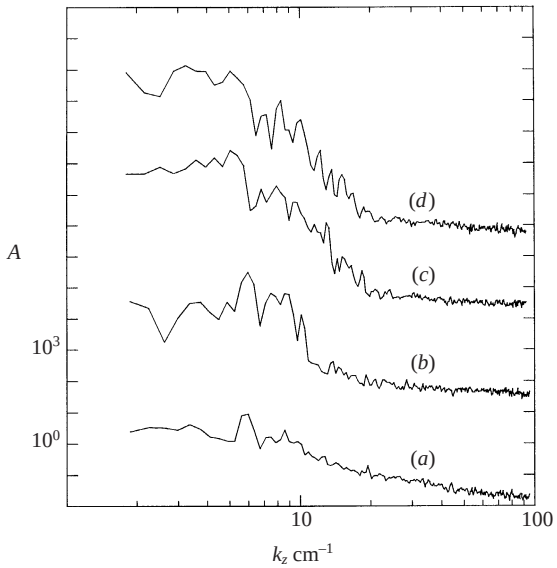

FIGURE 6. Wavenumber power spectra of spanwise distributions of the normalized surface temperature ($q'' = 2260\,\mathrm{W\,m^{-2}}$ and $\theta = 24°$) at (*a*) $G^* = 390$, (*b*) 510, (*c*) 610 and (*d*) 700.

range of experimental conditions, $\hat{\Phi}$ does not exceed 0.12 at the surface. The data of Shaukatullah & Gebhart (1978) show (dimensionless) disturbance levels as high as 1 within the boundary layer; however, in accord with linear stability analysis, the disturbance amplitude at the surface is significantly lower than within the boundary layer. At equivalent heat flux and inclination angles, the streamwise amplification rate of the present surface temperature disturbances is in good agreement with the measurements of Shaukatullah & Gebhart (1978) within the boundary layer. At a heat flux of approximately $2300\,\mathrm{W\,m^{-2}}$, the streamwise growth rates of the temperature disturbance β_T in both the present and earlier experimental investigations are generally in good agreement. However, in the present experiments, β_T is somewhat more sensitive to the inclination angle (for the present data $\beta_T = 0.064$, 0.11 and 0.2 whereas in the experiments of Shaukatullah & Gebhart (1978) $\beta_T = 0.075$, 0.11 and 0.17 for $\theta = 14°, 19°$, and 29°, respectively).

Wavenumber power spectra of spanwise temperature distributions at a number of streamwise locations (each displaced by three decades) are shown in figure 6. At $G^* = 390$ (figure 6*a*), there is a spectral peak at $k_z = 2\pi/\lambda = 5.8\,\mathrm{cm^{-1}}$ having an amplitude $A = 9.2$. The magnitude of this spectral peak increases to 1811 by $G^* = 610$ (figure 6*b*) and the amplification is accompanied by a significant spectral broadening within the band $1.9 < k_z < 12.6\,\mathrm{cm^{-1}}$. However, at $G^* = 700$ (figure 6*d*), spectral components around the subharmonic wavenumber $k_z \approx 3$ are amplified while the fundamental wavenumber is decaying. This spectral shift is evidence of the appearance of a subharmonic mode that is associated with the presence of merged or nearly merged streamwise vortices (cf. figure 3*c*).

The spanwise vortex wavelength inferred by Shaukatullah & Gebhart (1978) from their data is also compared to the vortex wavelength that is inferred from the present data. From figure 6 ($\theta = 24°$, $q'' = 2260\,\mathrm{W\,m^{-2}}$), the wavelength of the primary temperature disturbance λ_T is 1.08 cm so the vortex wavelength is $\lambda_v \approx 0.54\,\mathrm{cm}$ while Shaukatullah & Gebhart (1978) report $\lambda_v \approx 0.53\,\mathrm{cm}$ for $\theta = 19°$, and 29°

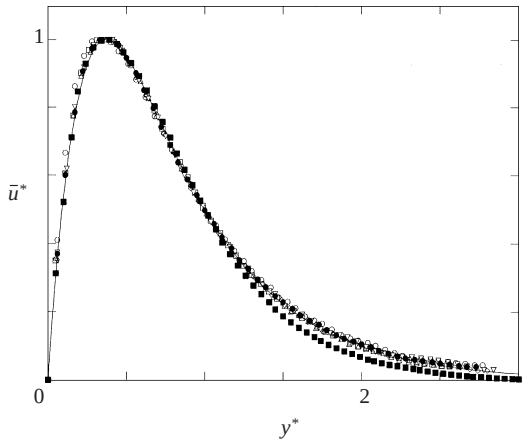

FIGURE 7. Cross-stream distributions of the spanwise-averaged streamwise velocity for $\theta = 14°$: $G^* = 400$ (○), 693 (□), $\theta = 19°$: $G^* = 408$ (◇), 540 (△), and $\theta = 24°$: $G^* = 364$ (▽), 444 (●), and 540 (■). The distribution for the two-dimensional laminar flow (vertical plate) is also shown for reference (——).

at $q'' \approx 2300\,\mathrm{W\,m^{-2}}$. As shown by Sparrow & Husar (1969), for a range of heat flux that also includes the present measurements, the spanwise vortex wavelength is virtually independent of the inclination angle. Therefore, it can be argued that the spanwise vortex wavelength that is estimated from the present liquid crystal surface temperature measurements is almost identical to the wavelength that was observed by Shaukatullah & Gebhart (1978).

The streamwise changes in surface thermal transport are clearly linked to the flow within the wall boundary layer. Figure 7 shows cross-stream distributions of the dimensionless spanwise-averaged streamwise velocity $\bar{u}^*$ (normalized by the maximum velocity $\bar{u}_{max}$), as a function of the dimensionless cross-stream variable y^* (normalized by the outer cross-stream elevation where $\bar{u} = 0.5\bar{u}_{max}$) for a number of inclination angles and streamwise stations. It is remarkable that, with the exception of the outer flow at $G^* = 540$ and $\theta = 24°$, the measured velocity distributions are virtually indistinguishable from the two-dimensional steady laminar solution (for $Pr = 5.8$). The streamwise position where the outer flow deviates from the laminar solution ($G^* = 540$, $\theta = 24°$) is within the domain where $Nu_x(Gr_x^*)$ also exhibits transitional behaviour (cf. figure 4).

As noted in § 2.1, spanwise temperature gradients that are induced by discrete spanwise heating on an inclined heated plate result in the production of streamwise vorticity Ω_x of prescribed magnitude and sense within the wall boundary layer. Therefore, it is expected that counter-rotating vortex pairs are formed between adjacent local spanwise temperature maxima or minima. Figures 8(*a*) and 8(*b*) show time-averaged cross-stream distributions of the (dimensionless) streamwise (u^*) and cross-stream (v^*) velocity components that are clearly consistent with the presence of counter-rotating streamwise vortices centred around maxima or minima of the spanwise temperature distributions imposed by the surface heaters. These data show that for $y^* < 1.5$, the cross-stream velocity is positive (i.e. away from the surface) at spanwise positions where the surface temperature has a local maximum, and negative (i.e. towards the surface) where the surface temperature has a local minimum. Concomitantly, the streamwise velocity and the boundary-layer thickness increase when the cross-stream velocity is positive and vice versa when the cross-stream velocity is

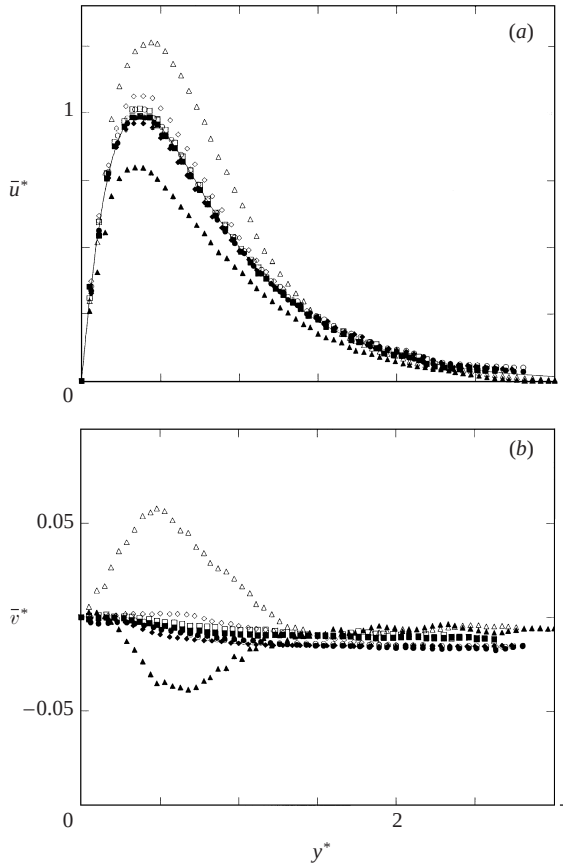

FIGURE 8. Cross-stream distributions of (*a*) streamwise and (*b*) cross-stream velocity components measured at spanwise maximae (open symbols) and minimae (closed symbols) of the surface temperature for $G^* = 408$, $\theta = 19°$ (○, ●), $G^* = 540$, $\theta = 19°$ (□, ■), $G^* = 364$, $\theta = 24°$ (◇, ◆), and $G^* = 540$, $\theta = 24°$ (△, ▲). The theoretical two-dimensional laminar flow (——).

negative. The thermal boundary layer undergoes similar changes because negative v^* indicates the transport of relatively cool ambient fluid toward the surface, whereas positive v^* indicates the advection of warmer fluid away from the surface. It is apparent that the transport of warmer fluid from the surface leads to an increase in the local streamwise velocity whereas the transport of cooler fluid towards the surface tends to slow the flow. Furthermore, at spanwise positions where the local streamwise velocity is lower, the local surface heat transfer rate is maximum (i.e. a local temperature minimum). In fact, in the early stages of the vortex evolution, the local Nusselt number at spanwise positions where the streamwise velocity has a local maximum is lower than in the two-dimensional flow. Thus, the surface heat transfer is strongly influenced by the magnitude and sign of the cross-stream velocity v^* within the boundary layer.

4. Time-invariant spanwise forcing

The flow features associated with the appearance of streamwise vortices at increasing inclination angles (figure 3*c*) are substantially enhanced when the spanwise

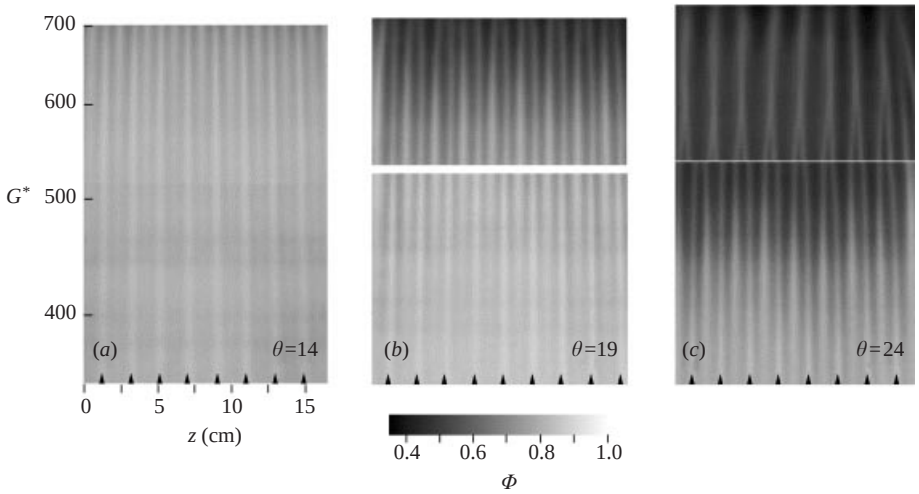

FIGURE 9. Surface temperature maps of the forced flow for $q'' = 2260\,\mathrm{W\,m^{-2}}$ and (*a*) $\theta = 14°$, (*b*) 19° and (*c*) 24°. Arrows mark the spanwise locations of the active actuators and the streamwise position of the actuators is at $G^* \approx 245$ (upstream from the arrows on the images).

instability that leads to their appearance is deliberately forced. In the present experiments, a single spanwise row of 32 heating elements (each extending between $x = 3\,\mathrm{cm}$ and 12.2 cm) is used to excite spanwise periodic instabilities whose spanwise wavelengths are discretized by activation of desired patterns of heating elements.

4.1. *Heat transfer*

Similar to figure 3, figures 9(*a*)–9(*c*) are composite grey scale raster plots of normalized surface temperature Φ of the forced flow for inclination angles $\theta = 14°, 19°$ and 24° ($q'' = 2260\,\mathrm{W\,m^{-2}}$). The spanwise excitation wavelength discretized by three actuators having a Boolean shape factor $S_3 = [1,0,0]$ is $\lambda = 1.9\,\mathrm{cm}$ and the relative forcing amplitude is $Q_r = 0.16$. The spanwise position of each active heating element is marked by an arrow on the horizontal axis (note that the actuators are actually located about 10 cm upstream of the bottom edge of the image at $G^* \approx 245$). Figures 9(*a*)–9(*c*) clearly demonstrate that the actuation results in the formation of high-temperature streaks at the spanwise forcing wavelength which persist throughout the downstream end of the measurement domain. Observations of earlier investigators (e.g. Shaukatullah & Gebhart 1978) as well as the present velocity measurements confirm that the high-temperature streaks (that coincide with the centre of the actuator) are associated with the upwash flow that is induced between streamwise counter-rotating vortex pairs. The low temperature streaks (between the actuators) are induced by the downwash flow which brings cooler fluid from above the thermal boundary layer towards the plate. Each vortex pair is formed by the equal and opposite spanwise temperature gradients that are imposed on either side of the heating element, and the spacing between adjacent pairs is determined by the wavelength of the excitation waveform.

An important feature of the temperature maps at $\theta = 14°$ and 19° (figures 9*a* and 9*b*) is the appearance of secondary high-temperature streaks between the existing streaks at $G^* \approx 520$ and 360 for $\theta = 14°$ and 19°, respectively. These secondary streaks apparently result from the formation of new pairs of counter-rotating streamwise vortices between existing adjacent forced pairs. At the downstream edges of both images, the secondary streamwise vortices appear to have the same strength as the

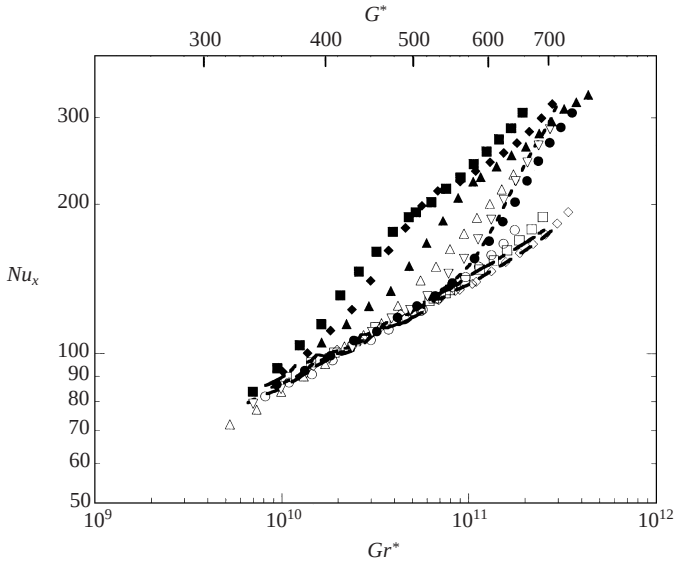

FIGURE 10. Heat transfer for the forced flow ($\lambda = 1.9$ cm); $\theta = 14°$: q_1'' (○), q_2'' (□), q_3'' (◇); $\theta = 19°$: q_1'' (△), q_2'' (▽), q_3'' (●); $\theta = 24°$; q_1'' (■), q_2'' (◆), q_3'' (▲). The unforced flow: (q_2'') $\theta = 14°$ (- - -), 19° (– – –) and 24° (- - - -). ($q_1'' = 1380$, $q_2'' = 2260$, $q_3'' = 3800\,\mathrm{W\,m^{-2}}$).

primary vortices, and the spanwise wavelength of the forced instability is effectively halved. Although the spanwise variations in the normalized surface temperature $\Phi(G^*, z)$ at $\theta = 14°$ are relatively weak (increasing from 1.6% at $G^* = 480$ to 3.2% at $G^* = 690$), they increase with inclination angle (to a maximum of 7.6% at $G^* = 645$ for $\theta = 19°$ and 9.1% at $G^* = 480$ for $\theta = 24°$). The spanwise variations in $\Phi(G^*, z)$ are accompanied by a general decrease in the spanwise-averaged surface temperature $\bar{\Phi}(x)$ (e.g. for $G^* = 570$: $\bar{\Phi} = 0.79$, 0.68 and 0.50 for $\theta = 14°, 19°$ and 24°, respectively) corresponding to an increase in the local heat transfer rate. Another notable feature of the flow is the merging of primary and secondary vortex pairs in figure 9(*c*) ($\theta = 24°$) at $G^* = 560$, which results in the doubling of the spanwise wavelength back to the forcing wavelength $\lambda = 1.9$ cm.

The dependence of Nu_x on Gr^* for the forced flow at $\theta = 14°$, 19° and 24° (each for three levels of surface heat flux) is shown in figure 10. The corresponding data for the unforced flow (at $q'' = 2260\,\mathrm{W\,m^{-2}}$) are also included for reference (dashed lines). In the unforced flow, Nu_x is virtually invariant with respect to θ at 14° and 19° and up to $G^* \approx 570$ at $\theta = 24°$. The natural appearance of streamwise vortices for $G^* > 570$ leads to a substantial increase in Nu_x. The data for the unforced and forced flows at $\theta = 24°$ indicate that the domain of influence of the forcing is $360 < G^* < 715$. Within this domain, Nu_x increases by as much as 170% (at $G^* = 570$) relative to the unforced flow at the same q''. However, at the downstream end of this domain, the Nusselt numbers of the unforced and forced flows (at $\theta = 24°$) become comparable as a result of the natural amplification of streamwise vortices in the unforced flow. As shown in figure 10, the domain of influence of the forcing at $\theta = 19°$ begins at larger G^* compared to $\theta = 24°$. The present data also show that for a given inclination angle, the magnitude of G^* at which transition occurs decreases with increasing levels of the dimensionless forcing amplitude Q_r. Because the power to the actuators in each case is identical, Q_r is effectively higher at lower q'' so that for $\lambda = 1.9$ cm, $Q_r = 0.26$, 0.16, and 0.10 for $q'' = 1380$, 2260 and $3800\,\mathrm{W\,m^{-2}}$, respectively.

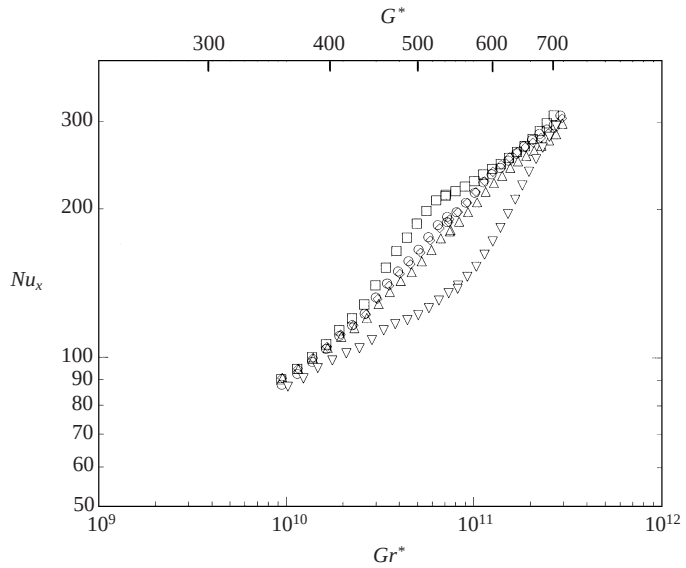

FIGURE 11. Heat transfer for $q'' = 2260\,\mathrm{W\,m^{-2}}$ and $\theta = 24°$: $\lambda_2 = 1.27\,\mathrm{cm}$ ($Q_r = 0.25$, ○), $\lambda_3 = 1.9\,\mathrm{cm}$ ($Q_r = 0.16$, □), $\lambda_4 = 2.5\,\mathrm{cm}$ ($Q_r = 0.12$, ◇), and $\lambda_5 = 3.2\,\mathrm{cm}$ ($Q_r = 0.1$, △). The unforced flow is marked by ▽.

The dependence of Nu_x on the spanwise wavelength of the excitation waveform is shown in figure 11 for $\theta = 24°$ and $q'' = 2260\,\mathrm{W\,m^{-2}}$. The excitation waveforms are given by groups of actuators having N elements and a spanwise wavelength λ_N with a single active actuator and decreasing duty cycle $\hat{d}_N$: $\lambda_2 = 1.27\,\mathrm{cm}$ ($S_2 = [1,0]$, $\hat{d}_2 = 0.5$), $\lambda_3 = 1.9\,\mathrm{cm}$ ($S_3 = [1,0,0]$, $\hat{d}_3 = 0.33$), $\lambda_4 = 2.5\,\mathrm{cm}$($S_4 = [1,0,0,0]$, $\hat{d}_4 = 0.25$) and $\lambda_5 = 3.2\,\mathrm{cm}$ ($S_5 = [1,0,0,0,0]$, $\hat{d}_5 = 0.2$). The data in figure 11 show that Nu_x is maximized for the forcing wavelength $\lambda_3 = 1.9\,\mathrm{cm}$ for which the relative forcing amplitude is $Q_r = 0.16$. Although Q_r decreases with spanwise wavelength, it appears that the heat transfer for the other wavelengths is similar and considerably larger than for the unforced flow. It is conjectured that at $\lambda_3 = 1.9\,\mathrm{cm}$ the spanwise spacing for the streamwise vortex pairs is optimal in the sense that it allows for more efficient surface cooling. Thus, the global (streamwise-averaged) increase in surface heat transfer rate is computed for this 'optimal' wavelength by considering the relative increment in the streamwise-averaged Nusselt number:

$$\Delta\overline{Nu}_x \equiv \frac{\displaystyle\int_0^x (h_{xF} - h_{xUF})\,\mathrm{d}x}{\displaystyle\int_0^x h_{xUF}\,\mathrm{d}x}$$

where h_{xF} and h_{xUF} are the spanwise averaged heat transfer coefficients for the forced and unforced flow, respectively. The variation of $\Delta\overline{Nu}_x$ with G^* (and Gr^*) for several levels of surface heat flux and inclination angles is shown in figure 12. In each case, $\Delta\overline{Nu}_x$ is nominally zero until the local strength of the forced streamwise vortices is sufficient to augment the local surface heat transfer. The streamwise rate of increase of $\Delta\overline{Nu}_x$ is initially positive and farther downstream it diminishes and eventually vanishes. The nominal streamwise position where the increase in heat transfer in the forced flow finally subsides, coincides with the streamwise domain where the

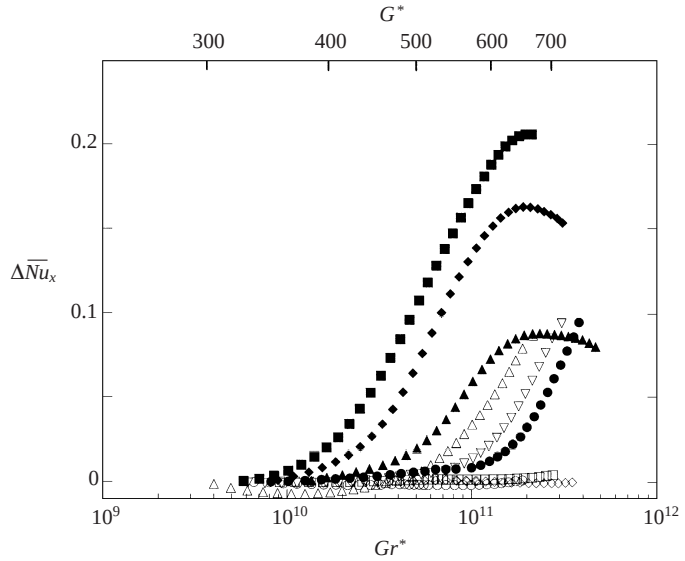

FIGURE 12. Variation of $\Delta\overline{Nu}_x$ with Gr^* for $\lambda = 1.9\,\text{cm}$ and $\theta = 14°$: q_1'' (○), q_2'' (□) and q_3'' (◇); $\theta = 19°$: q_1'' (△), q_2'' (▽) and q_3'' (●); and $\theta = 24°$; q_1'' (■), q_2'' (◆) and q_3'' (▲).

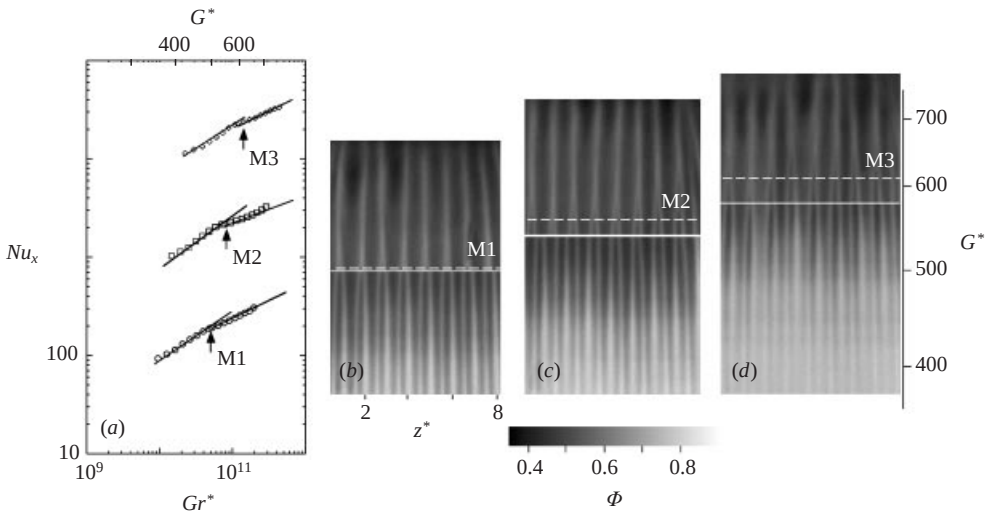

FIGURE 13. (*a*) Streamwise variation of Nu_x for $\theta = 24°$, $\lambda = 1.9\,\text{cm}$ and ○, $q'' = 1380\,\text{W m}^{-2}$; □, $2260\,\text{W m}^{-2}$; ◇, $3370\,\text{W m}^{-2}$. (*b–d*) The corresponding normalized surface temperature maps.

naturally occurring streamwise vortices in the unforced flow are sufficiently strong to effect thermal transport at a level that is equivalent to that of the forced flow. At an inclination angle of 24° and the highest forcing amplitude ($Q_r = 0.26$), a net increase in the global heat transfer rate of up to 20% is realized. Furthermore, as shown in figure 12, $\Delta\overline{Nu}_x$ decreases with the relative forcing amplitude and at smaller inclination angles the range of forcing effectiveness is shifted to larger G^*.

Although the average increase in the Nusselt number for the forced flow results from the addition of thermal energy by the actuators, the data of figure 12 show that this additional energy does not adversely affect the global heat removal. Compared to

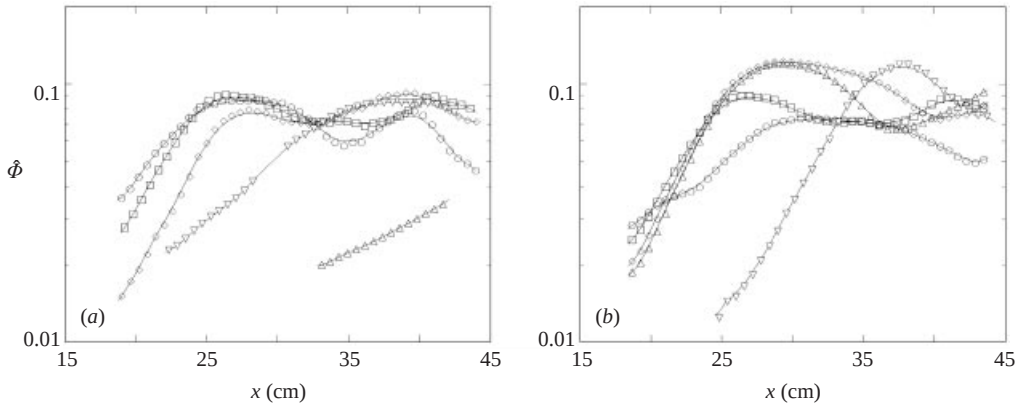

FIGURE 14. Streamwise variation of $\hat{\Phi}$: (*a*) $\lambda = 1.9$ cm and q_1'', θ_3 (○), q_2'', θ_3 (□), q_3'', θ_3 (◇), q_2'', θ_1 (△), q_2'', θ_2 (▽). (*b*) q_2'', θ_3 and $\lambda = 1.27$ (○), 1.9 (□), 2.5 (◇), 3.2 cm (△), and unforced (▽). ($q_1'' = 1380$, $q_2'' = 2260$, $q_3'' = 3800$ W m^{-2} and $\theta_1 = 14°$, $\theta_2 = 19°$, and $\theta_3 = 24°$.)

the unforced flow, more energy is removed from the surface when the flow is forced and at a lower average surface temperature.

The merging of adjacent streamwise vortices (figure 9*c*) is accompanied by a change in the rate of increase of the surface heat transfer. Figure 13(*a*) shows the streamwise variation of Nu_x for $\theta = 24°$ and $q'' = 1380$, 2260 and 3370 W m^{-2} (for clarity, the data at $q'' = 2280$ and 3370 W m^{-2} are displaced by one and two decades, respectively). These data show a distinct reduction in the slope of Nu_x at $G^* = 500$, 550 and 610 (marked by the arrows) for $q'' = 1380$, 2260 and 3370 W m^{-2}, respectively. The corresponding temperature maps in figures 13(*b*)–13(*d*) show that the reduction in the rate of increase of heat transfer begins where vortex merging occurs. Even though the circulation of the merged streamwise vortices is larger than the circulation of the individual vortices prior to merging, the reduction in the rate of increase of heat transfer appears to be caused by the reduced number of vortices following merging. Furthermore, the core centres of the stronger merged vortices are located at higher cross-stream elevations from the surface (see figure 25). It should also be noted that the increase with q'' in the streamwise location (G^*) of merging is a manifestation of the decrease in Q_r at higher heat flux levels.

4.2. *Disturbance amplification*

Although the forcing leads to an increase in the average heat transfer, it is also accompanied by stronger non-uniformities of the surface temperature (and thermal transport) compared to the unforced flow. Streamwise variations of the spanwise temperature variance $\hat{\Phi}$ are shown in figures 14(*a*) and 14(*b*) for several inclination angles, surface heat flux and forcing levels. In figure 14(*a*), the spanwise excitation results in an exponential growth in $\hat{\Phi}$ (which increases with inclination angle), indicating that the forced disturbances are initially amplified by a linear mechanism. Farther downstream, the amplification becomes nonlinear, the growth rates (at $\theta = 19°$ and 24°) decrease, and $\hat{\Phi}$ saturates and decays. For a given surface heat flux, the characteristic location of transition to nonlinear growth (i.e. the location of the saturation peak) decreases with the inclination angle. For example, at $q'' = 2260$ W m^{-2} and $\theta = 24°$, $\hat{\Phi}$ saturates at $x = 26$ cm ($G^* = 510$), whereas for $\theta = 19°$ the saturation occurs farther downstream at $x = 37$ cm ($G^* = 670$), and for $\theta = 14°$ saturation occurs downstream of the measurement domain. Figure 14(*b*) shows that, except for

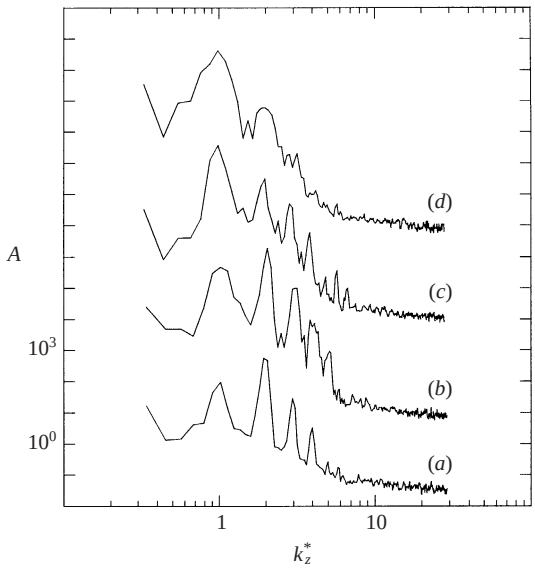

FIGURE 15. Wavenumber power spectra of the surface temperature in the forced flow for $q'' = 2260\,\mathrm{W\,m^{-2}}$, $\theta = 24^\circ$ and $\lambda = 1.9\,\mathrm{cm}$ at (*a*) $G^* = 390$, (*b*) 510, (*c*) 610 and (*d*) 700.

$\lambda = 1.27\,\mathrm{cm}$, the streamwise growth rate for different spanwise forcing wavelengths is similar to that of the unforced flow. For $\lambda = 1.27\,\mathrm{cm}$, the streamwise growth rate of $\hat{\Phi}$ is significantly lower than for the unforced flow ($0.08\,\mathrm{cm^{-1}}$ *vs.* $0.21\,\mathrm{cm^{-1}}$, respectively) and results in a smaller peak in $\hat{\Phi}$ (0.075 *vs.* 0.12, respectively). These data suggest that when large spanwise variations in scalar transport are undesirable (e.g. chemical vapour deposition), passive forcing at an appropriate wavelength can lead to relatively more uniform transport than in the unforced flow by deliberately inducing streamwise vortices having lower growth rate and saturation levels than the unforced vortices. A comparison of figures 5 and 14(*a*) shows that the maximum disturbance levels of surface temperature are approximately the same in the presence and absence of forcing. This suggests that the saturation mechanism for the disturbance is only weakly coupled to the source of the disturbance (i.e. forced vs. natural), but is strongly affected by the local disturbance amplitude.

Spanwise power spectra of the temperature map in figure 9(*c*) are computed using the normalized wavenumber $k_z^* = k_z\lambda$ (i.e. $k_z^* = 1$ is the forcing wavenumber) and plotted in figure 15 at several streamwise stations (as in figure 6, the spectra at successive streamwise locations are each displaced by three decades). The high-temperature secondary streaks that appear between forced streaks of the surface temperature in figure 9(*c*) correspond to spectral peaks at the first harmonic of the excitation wavenumber ($k_z^* = 2$). In fact, at the first measurement station ($G^* = 390$), the amplitude of the spectral peak at $k_z^* = 2$ is higher than the peak at the forcing wavenumber. The merging of streamwise vortices is accompanied by the streamwise decay of the spectral peaks at the harmonics of the forcing wavenumber, and at $G^* = 610$ the forced wavenumber is dominant again.

4.3. *The velocity field*

Distributions of the streamwise and cross-stream velocity in cross-stream (x, y)-planes of the forced flow are measured using particle image velocimetry (PIV). The measurements are taken at 32 cross-stream planes equally spaced within two forcing

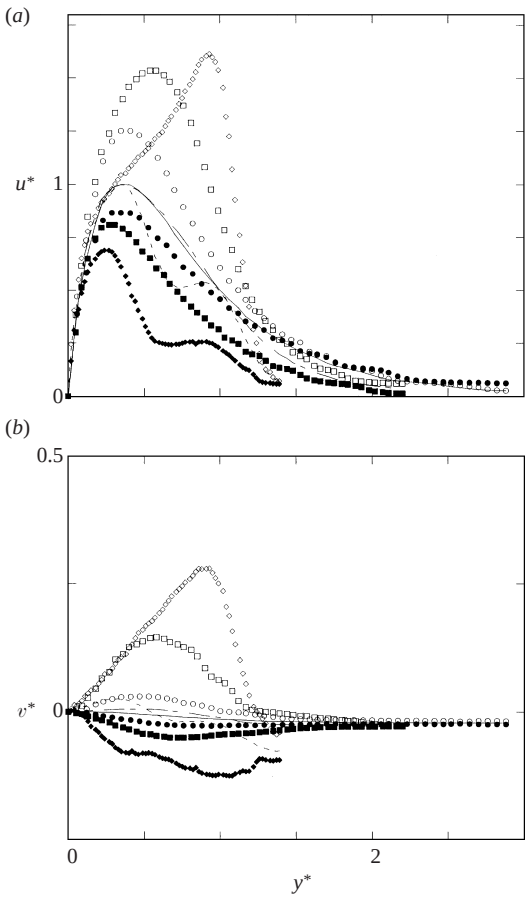

FIGURE 16. Cross-stream distributions of (*a*) the streamwise and (*b*) cross-stream velocity components measured at spanwise maximae (open symbols) and minimae (closed symbols) of the surface temperature for $\theta = 24°$, $q'' = 2260\,\mathrm{W\,m^{-2}}$, $\lambda = 1.9\,\mathrm{cm}$ and $G^* = 364$ (○, ●), 444 (□, ■), and 540 (◇, ◆); Spanwise-averaged distributions of $\bar{u}^*$ and $\bar{v}^*$ at $G^* = 364$ (—), 444 (— -), and 540 (- - - -) are also shown.

wavelengths. Distributions of the (dimensionless) streamwise and cross-stream velocity components in cross-stream planes at spanwise locations of maxima and minima of the surface temperature (cf. figure 9(*c*) for $\theta = 24°$, $q'' = 2260\,\mathrm{W\,m^{-2}}$, and $\lambda = 1.9\,\mathrm{cm}$) are shown in figures 16(*a*) and 16(*b*). Similar to figure 8 (the unforced flow), the cross-stream velocity v^* near the surface is positive (i.e. away from the surface) and negative (i.e. towards the surface) where the surface temperature has local maxima and minima, respectively, indicating the direction of the flow induced by streamwise counter-rotating vortex pairs. In contrast to the distributions in figure 8, positive velocity peaks of v^* in figure 16(*b*) are considerably larger than the negative peaks, ostensibly because of the spanwise locking of the streamwise vortices to the excitation wavelength. It is reasonable to argue that the buoyancy force induced by surface heating aids in the transport of fluid away from the surface. This effect is also evident in the corresponding distributions of the streamwise velocity (figure 16*a*) which have large cross-stream maxima where v^* is positive and indicate that the presence of the streamwise vortices leads to a thicker momentum (and thermal) boundary layer above spanwise positions of surface temperature maxima.

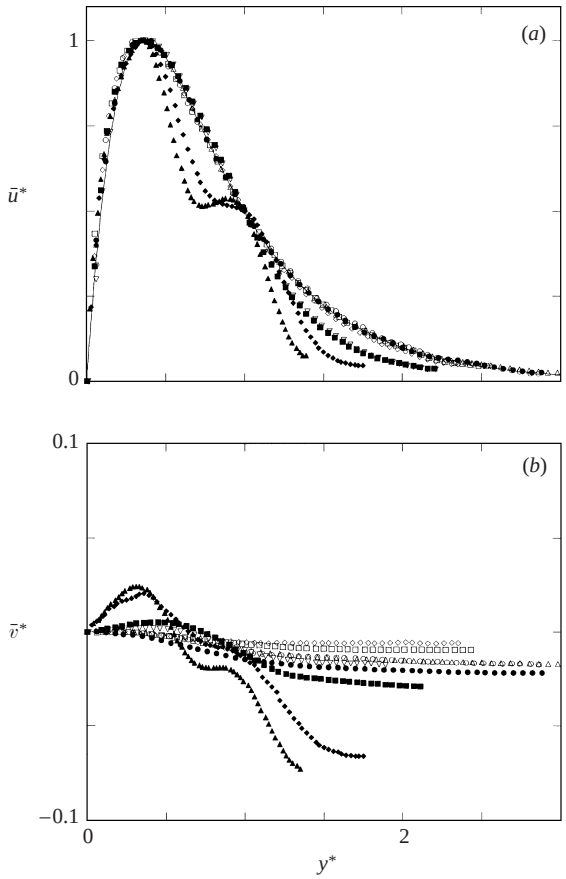

FIGURE 17. Cross-stream distributions of (*a*) the spanwise-averaged streamwise and (*b*) cross-stream velocity components for $\lambda = 1.9$ cm and three inclination angles: $\theta = 14°$: $G^* = 400$ (○), 545 (□), 693 (◇); $\theta = 19°$: $G^* = 408$ (△), 540 (▽); $\theta = 24°$: $G^* = 364$ (●), 444 (■), 515 (◆) and 540 (▲). The corresponding distribution of the streamwise velocity for the two-dimensional vertical laminar flow ($Pr = 5.8$) are shown using a solid line.

Figures 17(*a*) and 17(*b*) show cross-stream distributions of the spanwise-averaged streamwise ($\bar{u}^*$) and cross-stream ($\bar{v}^*$) velocities for $q'' = 2260\,\mathrm{W\,m^{-2}}$ and $\lambda = 1.9$ cm. At an inclination angle of 14° within the domain $G^* < 700$, the distributions of the streamwise velocity are similar to the theoretical two-dimensional laminar distribution and the corresponding cross-stream velocity (figure 17*b*) decreases monotonically from zero at the wall to a small negative value ($\bar{v}^* > -0.02$) outside the boundary layer. At $\theta = 19°$, the cross-stream width of the streamwise velocity distribution is narrower than in the corresponding laminar distribution for $G^* = 540$ and $y^* > 1.0$, and the cross-stream velocity becomes slightly positive at $y^* = 0.5$. As discussed in connection with figure 9(*a*) ($\theta = 19°$ and $q'' = 2260\,\mathrm{W\,m^{-2}}$), this is the streamwise location of the onset of transition in heat transfer. When the inclination angle is increased to 24°, the distributions of $\bar{u}^*$ and $\bar{v}^*$ undergo significant changes. The streamwise velocity distributions at $G^* = 515$ and 540 are narrower above $y^* > 0.5$ and develop additional inflection points at $y^* \approx 0.95$. For $G^* = 540$, the cross-stream velocity increases from zero at the wall to approximately 0.025 at $y^* = 0.33$ before dropping to approximately −0.07 at the cross-stream edge of the measurement domain. The large

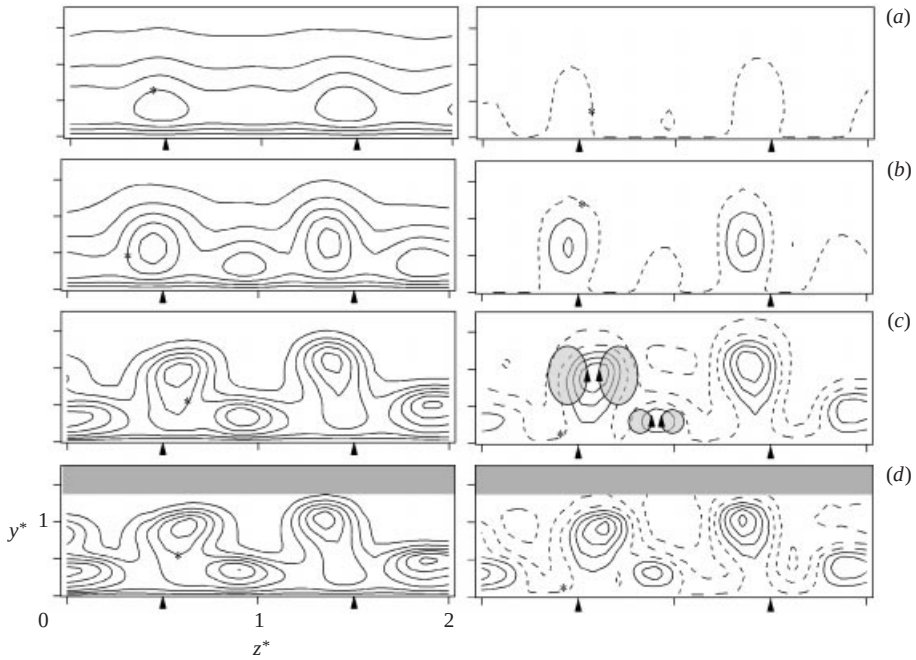

FIGURE 18. Contour maps of the streamwise (u^*, left) and cross-stream (v^*, right) velocity components in the (y^*, z^*) planes at (*a*) $G^* = 355$, (*b*) 435, (*c*) 515 and (*d*) 540. The contour levels 1 for u^* and 0 for v^* are marked with asterisks, and the respective contour increments are 0.25 and 0.05. The shaded rectangles in (*d*) mark the edges of the measurement domain. Arrows mark the spanwise location of the active actuators.

negative cross-stream velocity at the outer edge of the boundary layer is associated with the entrainment of lower-temperature ambient fluid into the boundary layer.

The evolution of a spanwise-periodic array of streamwise vortices can be inferred from pairs of contour maps of the dimensionless streamwise and cross-stream velocity components (u^* and v^*, respectively) in the (y^*, z^*)-plane ($z^* = z/\lambda$, $\lambda = 1.9\,\text{cm}$) at four streamwise stations $G^* = 355$, 435, 515 and 540 ($\theta = 24^\circ$, figures 18(*a*)–18(*d*), respectively). The spanwise locations of the active heating elements are marked by arrows for reference. (Recall that the actuators are located upstream at $G^* \approx 245$.) At the first streamwise measurement station ($G^* = 355$, figure 18*a*), the contour map of u^* shows spanwise periodic peaks in the streamwise velocity centred at $y^* = 0.33$ that are presumably buoyancy driven by the spanwise periodic heating (the spanwise location of the active actuators are aligned with the velocity peaks). The contour map of the cross-stream velocity v^* indicates that at the spanwise locations of the streamwise velocity peaks, there is a flow away from the surface. Farther downstream ($G^* = 435$ and 515, figures 18(*b*) and 18(*c*)), the spanwise peaks in the streamwise velocity intensify and are displaced farther away from the surface. The cross-stream displacement of the spanwise peaks away from the surface is manifested in a bulge at $y^* \approx 1$ in the corresponding spanwise-averaged streamwise velocity distribution of figure 17(*a*). Figures 18(*b*) and 18(*c*) also include contours of $v^* > 0$, indicating flow away from the surface at spanwise positions of the peaks in u^*. Moreover, the protrusion of these contours away from the surface suggests the formation of streamwise counter-rotating vortex pairs centred at $z^* = 0.58$, and 1.4 (the primary pair at $z^* = 0.58$ and $y^* = 0.9$ in figure 18(*c*) is marked by shading). The fluid that

is transported away from the surface is ultimately turned in the streamwise direction along with fluid that is transported towards the surface from the outer flow. The contour maps of v^* further show that the velocity field induced by each streamwise vortex of the pair is not symmetric about the centre of the vortex core (i.e. the cross-stream velocity away from the surface appears to be stronger than the velocity towards the surface). As argued in connection with figure 16, this is ostensibly the result of the bias imposed by a net buoyancy effect. Figures 18(b) and 18(c) also show the appearance of secondary streamwise vortices (e.g. at $z^* = 0.91$ and $y^* = 0.3$, as marked by the shaded circles) that are also apparent between the primary streaks in the temperature maps of figure 9(c). At $G^* = 540$ (figure 18d), the secondary vortex pairs begin to migrate closer to the primary vortices as a precursor to the merging between the primary and secondary vortices (cf. figure 9c).

In the absence of measurements of the transverse (spanwise) velocity component w, concentrations of streamwise vorticity $\Omega_x = \partial w/\partial y - \partial v/\partial z$ are approximated by $-\partial v/\partial z$. This approximation is justified by a comparison of the separate contributions of $\partial w/\partial y$ and $\partial v/\partial z$ to the total vorticity flux within the core of one of the counter-rotating streamwise vortices as measured by the circulation about the core. The circulation $\Gamma = \oint_C \boldsymbol{V} \cdot \mathrm{d}\boldsymbol{l}$ is computed along a contour C which is a rectangle in the (y, z)-plane that is bounded from below by the surface and its two sides intersect spanwise positions of adjacent maxima and minima of the cross-stream velocity. The top side of C is located well above the domain that contains streamwise vorticity where the spanwise velocity w is vanishingly small and therefore does not contribute to the circulation along C. The vorticity flux associated with $-\partial v/\partial z$ within the area that is bounded by C is computed from the data and is between 0.8 and 0.9Γ suggesting that the contribution of $|\partial w/\partial y|$ is significantly smaller than $|\partial v/\partial z|$. Although the quantity $\partial v/\partial z$ accounts for only part of the streamwise vorticity, it can be used to qualitatively describe the location and growth of the streamwise vortices.

Contour maps of (the dimensionless) $-\partial v^*/\partial z^*$ (figure 19) suggest the presence of spanwise-regular vortex pairs at $G^* = 435$ where the elevation of the centres of the vortex cores is $y^* = 0.55$. It appears that the pairs are slightly shifted to the left relative to the spanwise location of the active actuators (upstream), but maintain their spanwise spacing (at the forcing wavelength). At this streamwise station, the aspect ratio (height/width of a vortex) is nominally 1.7 and additional measurements (not shown) verify that it is relatively invariant with the plate inclination angle. At $G^* = 515$, the cores of the primary vortices are lifted farther above the surface to $y^* = 1$, ostensibly because of the increase in their strength and their self-induced velocity. The presence of the secondary streamwise vortices and their interaction with the primary vortices that ultimately leads to pairing of the primary and secondary vortices farther downstream (cf. figure 9c), results in a reduction in the spacing between the vortex pairs whereas the secondary vortices remain closer to the surface and well below the primary vortices. The interaction between the primary and secondary streamwise vortices intensifies farther downstream and at $G^* = 540$, the primary pair at $z^* = 0.6$ and the secondary pair on its right begin to merge.

The streamwise increase of the primary vortex circulation is shown in figure 20 for three inclination angles ($\lambda = 1.9$ cm, $Q_r = 0.167$ and $q'' = 2260\,\mathrm{W\,m^{-2}}$). Similar to the spanwise variance of the surface temperature ($\hat{\Phi}$ in figure 14), the streamwise growth rate of the vortex circulation increases with inclination angle (0.13, 0.19, $0.29\,\mathrm{cm^{-1}}$ for $\theta = 14^\circ$, 19°, 24°, respectively), and the initial exponential growth indicates that the vortices are amplified by a linear mechanism. Although the surface heating in the experiments of Zuercher *et al.* (1998) is different from that in the present work,

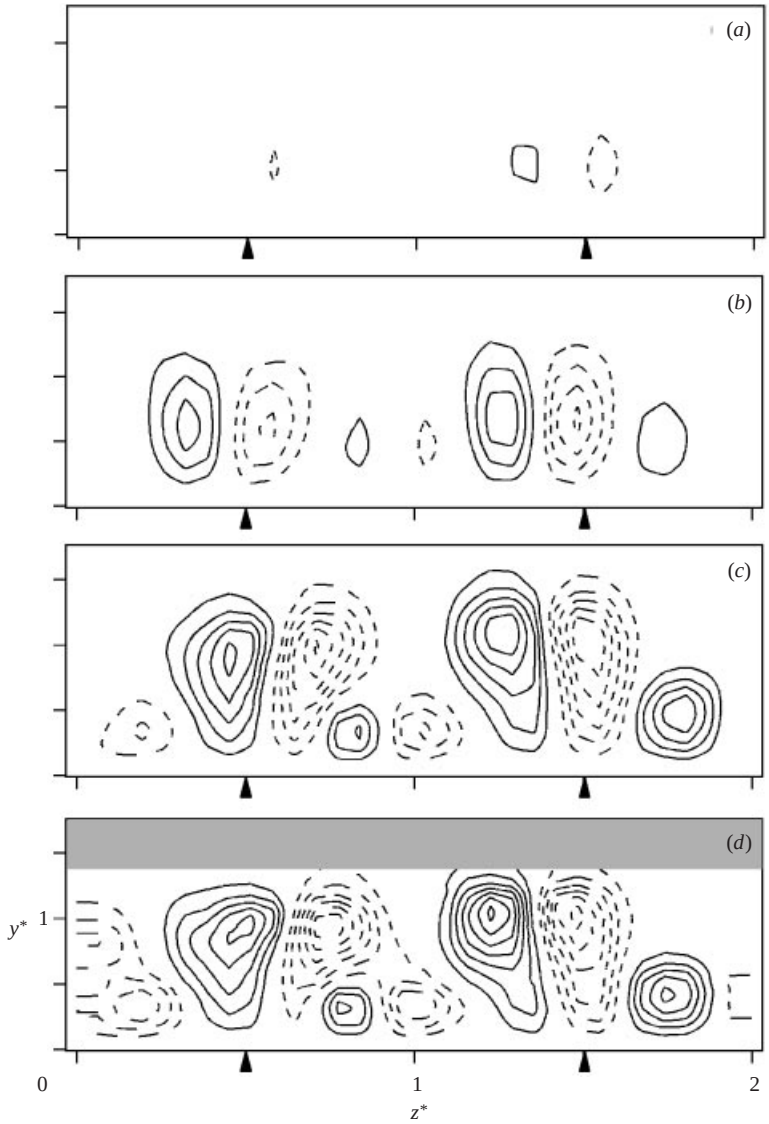

FIGURE 19. Contours of $-\partial v^*/\partial z^*$ in the (y^*, z^*)-planes at (*a*) $G^* = 355$, (*b*) 435, (*c*) 515 and (*d*) 540. Contour levels vary between -1.75 and 1.75 and the contour increment is 0.25. The shaded rectangular area in (*d*) marks the edge of the measurement domain.

their vortex circulation data for $\theta = 30^\circ$ and $\Delta T = 10\,^\circ\mathrm{C}$ are shown for comparison. Consistent with the observation that the disturbance growth rate is a strong function of inclination angle, the data of Zuercher *et al.* (1998) show that the streamwise growth rate of the vortex disturbance is $0.31\,\mathrm{cm}^{-1}$ and is somewhat larger than growth rates quoted above for the present experiments when $\theta \leqslant 24^\circ$. It is also apparent that the maximum magnitude of vortex circulation obtained before saturation is comparable in both investigations. Within the present measurement domain, the circulation begins to saturate only at $\theta = 24^\circ$ for $G^* > 450$ ($x > 23\,\mathrm{cm}$), which is also where $\hat{\Phi}$ begins to saturate for the same forcing conditions (figure 14*a*), indicating that the surface temperature disturbance is strongly linked to the circulation of the vortices.

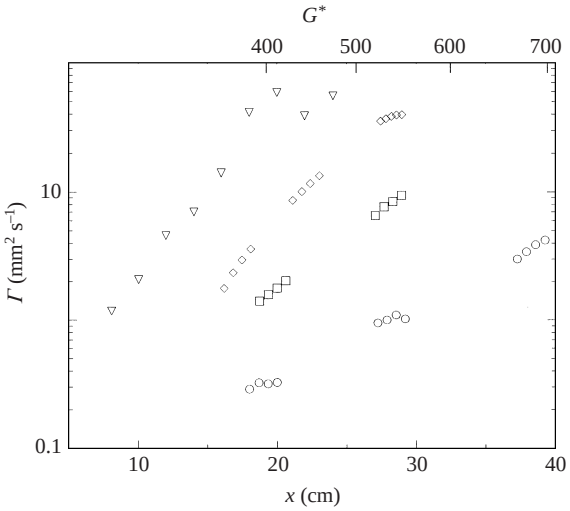

FIGURE 20. Vortex circulation for $q'' = 2260\,\mathrm{W\,m^{-2}}$, $\lambda = 1.9\,\mathrm{cm}$ and $\theta = 14^\circ$ (○), 19° (□) and 24° (◇). Circulation data from Zuercher *et al.* (1998) for $\Delta T = 10\,^\circ\mathrm{C}$ and $\theta = 30^\circ$ (△).

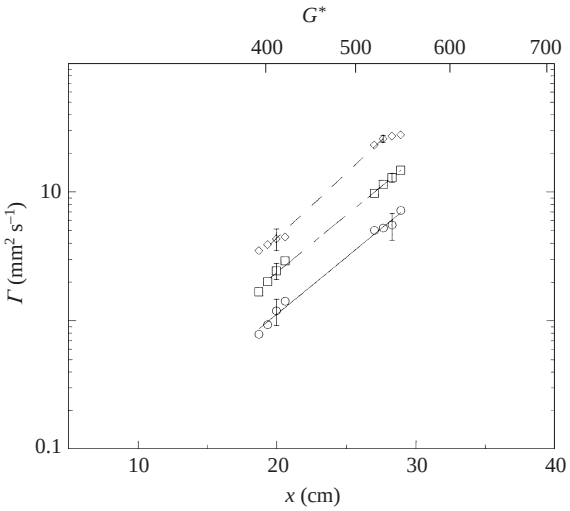

FIGURE 21. Vortex circulation for $q'' = 2260\,\mathrm{W\,m^{-2}}$, $\lambda = 1.27\,\mathrm{cm}$ and $\theta = 19^\circ$: $Q_r = 0.125$ (○), 0.25 (□) and 0.5 (◇).

The dependence of the vortex circulation on the forcing amplitude Q_r is shown in figure 21. These data show that doubling Q_r nominally doubles the circulation at a given streamwise position, and that at least during the early stages of the vortex growth the circulation behaves as $|\Gamma| = Q_r A_0 \mathrm{e}^{Bx}$ (A_0 and B are constant for a given surface heat flux, inclination angle, and actuator location). As demonstrated in § 4.5, the dependence of the spanwise position of the vortex and its strength on the location and magnitude (Q_r) of the actuation can be used to control cancellation or enhancement of the streamwise vortices.

It is apparent that the streamwise vortices augment thermal transport from the surface by increasing the net streamwise velocity (and the net volume flow rate) within the boundary layer. It can be shown that, for a two-dimensional laminar

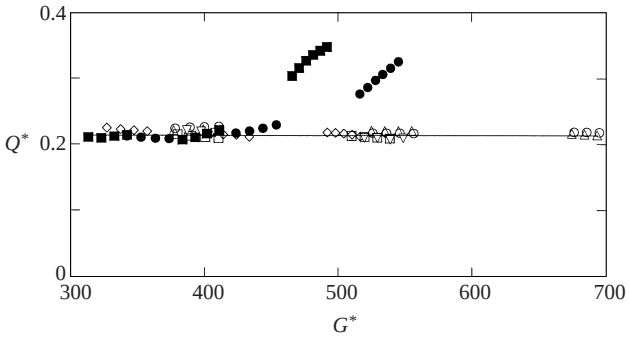

FIGURE 22. Streamwise variation of the spanwise-averaged flow rate Q^* ($q'' = 2260\,\mathrm{W\,m^{-2}}$): the unforced flow $\theta = 14°$ (○), 19° (□) and 24° (◇); the forced flow ($\lambda = 1.9\,\mathrm{cm}$) $\theta = 14°$ (△), 19° (▽), 24° (●); $q'' = 1380\,\mathrm{W\,m^{-2}}$ and $\theta = 24°$ (■); the two-dimensional laminar solution for $Pr = 5.8$ (—).

boundary layer, the Nusselt number is directly proportional to the streamwise flow rate ($Nu_x \propto vQ$), which implies that, in the absence of a secondary flow, higher flow rate results in larger Nu_x. However, in the presence of streamwise vortices this simple relationship between Nu_x and Q no longer holds locally. In fact, in contrast to the two-dimensional flow, at spanwise locations where the local streamwise flow rate is maximum (or minimum) the surface temperature is highest (or lowest). Nevertheless, it is found that a larger spanwise-averaged flow rate results in a larger spanwise-averaged Nusselt number. The streamwise variation of the spanwise-averaged dimensionless flow rate $Q^* = Q/(vG^*)$ for $\lambda = 1.9\,\mathrm{cm}$ and the corresponding flow rate for a laminar two-dimensional flow ($Q^* = 0.216$ for $Pr = 5.8$, i.e. Q increases linearly with G^*) are shown in figure 22. Within some range of G^*, Q^* in the forced flow ($\theta = 24°$ for both $q'' = 1380$ and $2260\,\mathrm{W\,m^{-2}}$) is indeed larger than in the two-dimensional flow. The deviation from the two-dimensional flow begins at $G^* = 420$ for $q'' = 2260\,\mathrm{W\,m^{-2}}$ and $G^* = 390$ for $q'' = 1380\,\mathrm{W\,m^{-2}}$ which correspond to the streamwise locations of transition in heat transfer in figure 10. The maximum Q^* is 0.35 which is 1.6 times higher than the flow rate for the two-dimensional laminar flow, and, as can be seen in figure 10, Nu_x in the forced flow is also approximately 1.6 times higher than in the two-dimensional flow. This result suggests that the increase in heat transfer rate is strongly linked to enhanced entrainment of ambient fluid by the three-dimensional flow.

4.4. *Vortex merging*

As discussed in § 4.1, adjacent pairs of streamwise vortices begin to merge downstream of where they first appear, resulting in substantial changes in the surface heat transfer (e.g. figures 13*a*–13*d*). Surface temperature maps within the domain of merging ($\theta = 24°$) for three forcing waveforms $\lambda_3 = 1.9\,\mathrm{cm}$, $S_3 = [1,0,0]$ and [1,1,0], and $\lambda_6 = 3.8\,\mathrm{cm}$, $S_6 = [1,1,1,0,0,0]$ are shown in figures 23(*a*)–23(*c*), respectively. Although the merging in figures 23(*a*) and 23(*b*) appear to be similar, only half the streamwise vortices in figure 23(*a*) are primary vortex pairs (i.e. triggered by an active heating element) and every other vortex pair is secondary (i.e. induced between the primary vortices), whereas all the streamwise vortices in figure 23(*b*) are primary vortices. Another distinction between the merging in figures 23(*a*) and 23(*b*) is that the merging in the former occurs farther downstream. It appears that when all the vortex pairs are forced (as in figure 23*b*), they are of equal strength

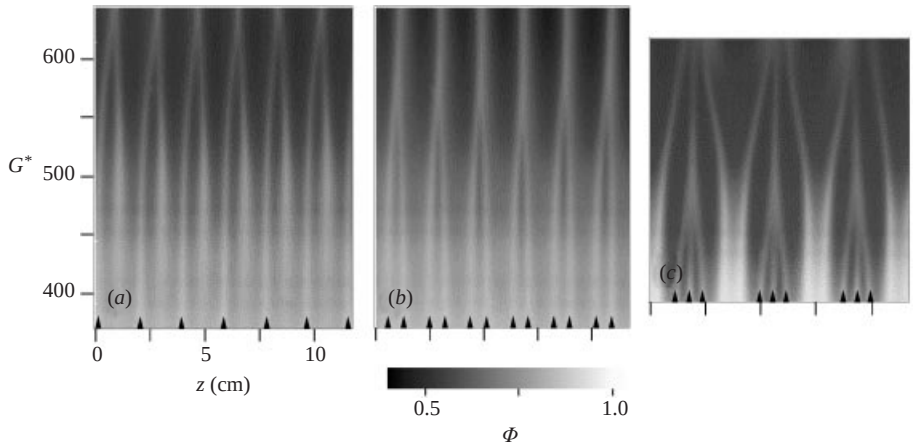

FIGURE 23. Surface temperature maps: (*a*) $\lambda_3 = 1.9\,\text{cm}$, $S_3 = [1,0,0]$, $Q_r = 0.21$, (*b*) $\lambda_3 = 1.9\,\text{cm}$, $S_3 = [1,1,0]$, $Q_r = 0.42$, and (*c*) $\lambda_6 = 3.8\,\text{cm}$, $S_6 = [1,1,1,0,0,0]$, $Q_r = 2$. Arrows mark the spanwise location of the active actuators ($q'' = 1760\,\text{W m}^{-2}$ and $\theta = 24^\circ$).

and begin to interact farther upstream, whereas the interaction of the primary and secondary vortices begins only when the secondary vortices become stronger farther downstream. The difference in strength of the primary and secondary vortices can be exploited to induce complex merging scenarios. For example, figure 23(*c*) shows two merging stages where three primary vortex pairs merge into a single vortex pair at $G^* = 450$, followed by the merging of the two secondary vortex pairs with the ensuing single primary vortex pair at $G^* = 620$. At this inclination angle, this two-stage merging is not observed in the unforced flow because a relatively higher forcing amplitude is required to produce the second merging. It is noteworthy that following the merging, the spanwise wavelength of the streamwise vortices is equal to the base wavelength of the forcing waveform (i.e. $\lambda_{merge} = \lambda_{forced} = 1.9\,\text{cm}$ in figures 23(*a*) and 23(*b*), and $\lambda_{merge} = \lambda_{forced} = 3.8\,\text{cm}$ in figure 23*c*). Other forcing patterns (not shown) have yielded similar results.

Nonlinear stability analysis for a natural convection flow over an inclined isothermal flat-plate (Chen *et al.* 1991) predicts that the merging of streamwise vortices occurs at a critical modified Reynolds number $\tilde{R}_{1/2}$ [$\tilde{R} = G^* \tan(\theta)$] which is independent of the inclination angle (e.g. for $Pr = 5.8$, $\tilde{R}_{1/2} = 41$). In the present experiments, $\tilde{R}_{1/2}$ (i.e. the merging location) is measured for a range of inclination angles, and several forcing amplitudes (figure 24). At each forcing level, $\tilde{R}_{1/2}$ increases with inclination angle and decreases with increasing forcing amplitude over the present range of θ. The data show that $\tilde{R}_{1/2}$ is only weakly dependent on θ, and that for a given forcing amplitude, $\tilde{R}_{1/2}$ increases by no more than 20% of its nominal value within the range $14^\circ < \theta < 40^\circ$. For the unforced flow, $\tilde{R}_{1/2}$ is shown for $\theta = 24^\circ$ and 29° suggesting that the critical merging location for a constant heat flux surface is $\tilde{R}_{1/2} \approx 290$. While the onset of the instability is outside the scope of the present work, the location of the onset $\tilde{R}_c$ is estimated from the work of Shaukatullah & Gebhart (1978) who investigated the unforced flow in detail and whose results are in good agreement with the present measurements. From their data, it is estimated that $\tilde{R}_c = 130$. Based on the present measurements, $\tilde{R}_{1/2} = 290$ and therefore $\tilde{R}_{1/2}/\tilde{R}_c = 2.2$ which is somewhat larger than the ratio that is determined from the analysis of Chen *et al.* (1991) for an isothermal surface condition ($\tilde{R}_{1/2}/\tilde{R}_c = \frac{41}{24.3} = 1.7$).

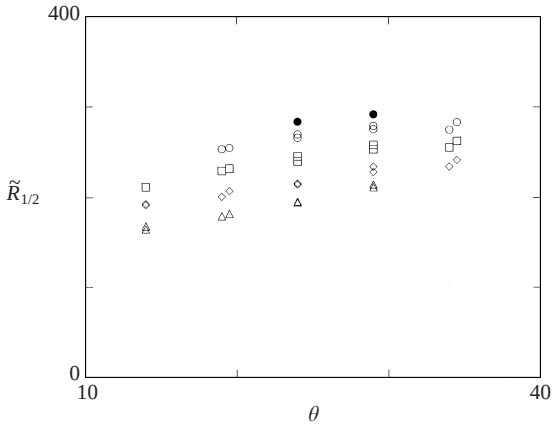

FIGURE 24. Location of vortex merging for $\lambda = 1.9\,\text{cm}$ and $Q_r = 0.25$ (○), 0.5 (□), 1 (◇), 2 (△) and unforced (●).

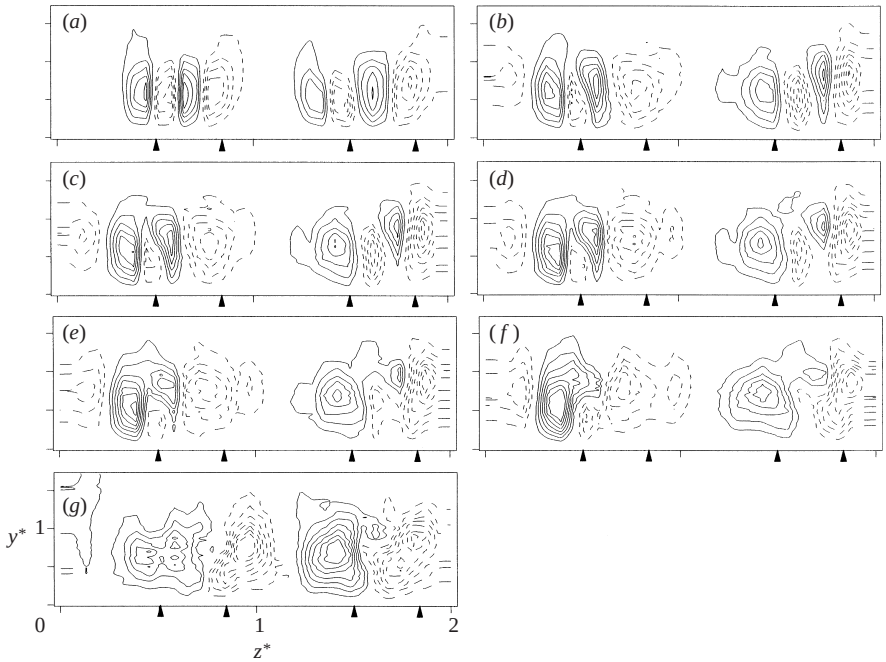

FIGURE 25. Contour maps of $-\partial v^*/\partial z^*$ in the (y^*, z^*)-planes for $\lambda_3 = 1.9\,\text{cm}$, $S_3 = [1, 1, 0]$, $q'' = 2260\,\text{W m}^{-2}$ and $\theta = 24°$. (*a*) $G^* = 427$, (*b*) 462, (*c*) 469, (*d*) 475, (*e*) 481, (*f*) 495 and (*g*) 507. Contour levels vary between −1.75 and 1.75 and the contour increment is 0.25. Arrows mark the spanwise locations of the active actuators.

Some details of the merging process are revealed by PIV measurements in the (y^*, z^*)-plane ($\theta = 24°$, $q'' = 2260\,\text{W m}^{-2}$, $\lambda = 1.9\,\text{cm}$ and $S_3 = [1, 1, 0]$). Figure 25 shows a sequence of contour maps of $-\partial v^*/\partial z^*$ before (*a*), during (*b–f*), and after (*g*) the merging is completed. Figure 25(*a*) ($G^* = 427$) shows two groups each comprised of two adjacent vortex pairs where solid contours represent counterclockwise (CCW) rotation. During the merging (figures 25*b*–25*e*, $G^* = 462$–481), the inner CCW vortex in each group of four vortices lifts above the inner CW vortex and moves to the left

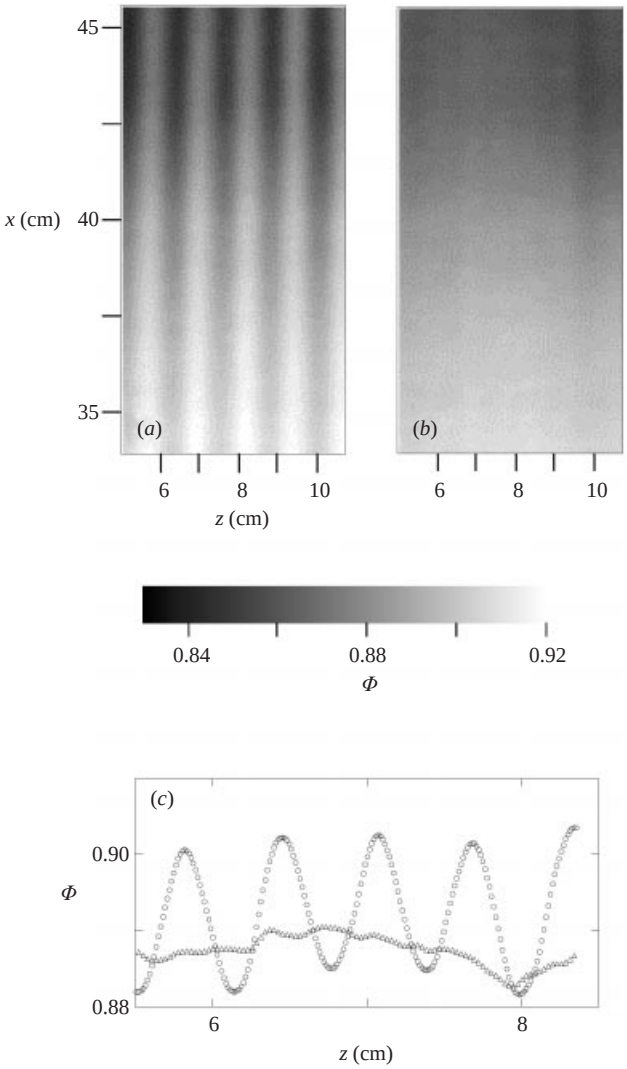

FIGURE 26. Surface temperature maps $\theta = 14°$, (a) the forced flow, (b) with activated cancellation actuators. (c) Spanwise distribution of the surface temperature; ○, the forced flow and △, with activated cancellation actuators (at $x = 39$ cm, $G^* = 670$).

while the inner CW vortex moves (underneath the CCW vortex) to the right. The merging of each of the two same-sign vortices on the left-hand side (CCW) and on the right-hand side (CW) is completed by counterclockwise motion of the pairs on the left- and right-hand sides.

4.5. *Controlled cancellation of flow instabilities*

The response of the flow to the application of discrete spanwise-periodic forcing suggests that this approach may be useful for the development of a control scheme that would delay the evolution of the streamwise instability. A simple implementation of this approach in which the surface actuators are used to suppress the evolution of the streamwise vortices is described below.

A system of streamwise vortices having a spanwise wavelength of 1.27 cm is forced

into the boundary layer with an upstream row of heating elements (at $x = 7.6$ cm, $G^* = 180$). The resulting distribution of surface temperature for this case is shown in figure 26(*a*). Because the origin of the disturbance is known *a priori*, a downstream row of actuators is used to cancel the imposed input disturbance. The downstream actuators are activated 2.5 cm downstream from the first row of actuators ($G^* = 230$) such that they are spatially out of phase, relative to the upstream row. This open-loop cancellation appears to be very promising, as can be seen in figure 26(*b*). The spanwise variations are almost entirely cancelled along the entire measurement domain beginning at 24 cm downstream from the cancellation actuators ($G^* = 600$). A plot of the spanwise temperature variations at $x = 39$ cm ($G^* = 670$) is shown for reference in figure 26(*c*). The peak-to-peak spanwise variations in temperature are decreased by a factor of four when the cancellation actuators are activated. It should be noted that the domain of influence of the present approach to the controlled cancellation of disturbances within the flow does not permanently stabilize the flow, and the streamwise vortices can reappear farther downstream. It is anticipated that future work will investigate the impact of vortex cancellation on time-varying flow transitions.

5. Concluding remarks

The evolution of streamwise vortical structures and their effect on heat transfer within the buoyancy-driven boundary layer over an inclined heated plate is investigated experimentally. In the absence of external forcing, nominally spanwise-periodic arrays of streamwise counter-rotating vortex pairs result from a three-dimensional instability of the base flow to spanwise non-uniformities in surface temperature at plate inclination angles that typically exceed 14°. The presence of each vortex pair is accompanied by corresponding spanwise excursions in surface temperature which alternate above and below the local spanwise-averaged temperature and appear as streamwise streaks in surface temperature maps. The high-temperature streaks are associated with the upwash flow that is induced between streamwise counter-rotating vortex pairs, whereas the low-temperature streaks result from the downwash flow which brings cooler fluid from above the thermal boundary layer towards the surface. This process intensifies as the strength of the counter-rotating streamwise vortices increases with downstream distance and the surface heat transfer increases compared to the (theoretical) heat transfer in the two-dimensional laminar base flow. The (dimensionless) streamwise location G^* where the surface heat transfer begins to deviate from the theoretical prediction for the two-dimensional flow is invariant with surface heat flux and moves upstream as the plate inclination angle is increased (relative to the vertical). The domain of influence of the forcing as manifested by an increase in the surface heat transfer (e.g. at $\theta = 24°$) is $360 < G^* < 715$.

In the present experiments, arrays of spanwise-periodic streamwise vortices with a prescribed spanwise spacing are deliberately triggered and manipulated by programmable spanwise-periodic variations in the surface temperature that are effected by linear (spanwise) arrays of discrete surface heating elements. The induced up- and down-wash flows between the counter-rotating vortex pairs are marked by high- and low-temperature streaks, respectively, that are aligned with the spanwise position of the active heating elements. The presence of the sreamwise vortices results in increased entrainment of lower-temperature ambient fluid into the boundary layer, leading to an increase in the spanwise-averaged volume flow rate and enhanced surface heat transfer. As a result of the forcing, the local Nusselt number Nu_x increases by as

much as 170% relative to the unforced flow (at the same surface heat flux) and the net increase in the global heat transfer at the largest forcing amplitude is about 20%. Following thermal transition in the unforced flow (e.g. $G^* \approx 550$, $\theta = 24^\circ$), the Nusselt numbers of the unforced and forced flows become comparable.

The cores of the streamwise vortices scale with the local thickness of the boundary layer, and when the forcing wavelength is larger than the characteristic diameter of the vortex core ($\lambda_f/\delta > 3$), secondary streamwise vortex pairs appear between the primary vortices. Spanwise merging between the primary and secondary vortices farther downstream results in a vortex system having a spanwise wavelength that is equal to the forcing wavelength, thus completing a cycle in which the wavelength of the vortex system is first doubled and then halved. The streamwise location of the merging depends primarily on the magnitude of vortex circulation where the merging of stronger vortices (induced by higher forcing amplitude) occurs farther upstream. The critical Reynolds number $\tilde{R}_{1/2}$ for vortex merging is only a weak function of the inclination angle and the merging of streamwise vortices in the unforced flow occurs farther downstream than is predicted by current nonlinear theory. Measurements of the surface temperature show that immediately downstream of the actuators, the instability that leads to the evolution of the streamwise vortices grows exponentially with streamwise distance indicating that, at least initially, the forced disturbances are amplified by a linear mechanism. Farther downstream, the streamwise amplification becomes nonlinear and the disturbance amplitude saturates and subsequently decays. Because the amplification of the instability increases with plate inclination angles, the domain of influence of the actuators shifts to a range of smaller G^* as the plate inclination angle is increased. The measurements also show that when the spanwise excitation wavelength increases (e.g. $\lambda_f/\delta > 3$), the streamwise amplification rate of the unforced and forced flows are virtually identical and that secondary streamwise vortices that are not triggered by the active heating elements appear between the forced primary vortices. However, at lower forcing wavelengths, the small spanwise spacing between the primary vortices inhibits the formation of unforced vortex pairs and the overall streamwise amplification rate is lower than in the unforced flow. In this case, the spanwise variance in surface temperature following the saturation of the forced disturbance is lower than in the unforced flow, implying a more spanwise-uniform heat transfer.

An important contribution of the present experiments is the demonstration that disturbances induced by spanwise arrays of discrete heating elements can be used to suppress the formation of naturally occurring streamwise vortices and thus maintain a nominally two-dimensional flow over an extended length of the heated surface. An array of streamwise vortices was seeded into the two-dimensional base flow and was subsequently cancelled by another array of actuators farther downstream, resulting in a substantial reduction in spanwise variations of the surface temperature. These results suggest that the evolution of the instabilities of the base flow can be actively controlled with the objectives of either maintaining the two-dimensionality of the base flow by delaying the appearance of the streamwise vortical structures or enhancing surface heat (and possibly mass) transport by exploiting enhanced entrainment of ambient fluid. The present experiments also demonstrate the suitability of arrays of surface-mounted heating elements and liquid crystal temperature sensors for future implementation of closed-loop control algorithms. Although optical diagnostics of liquid crystal surface thermometry may be cumbersome, their near-continuous spatial resolution provides a powerful tool for sensing the surface temperature over a broad range of spatial wavenumbers. An analysis similar to that developed by Joshi, Speyer

& Kim (1997) for plane Poiseuille flow may be applicable for the determination of optimal actuator layout, system controllability and observability criteria, and the selection of successful control algorithms.

Finally, similar to momentum boundary layers, the evolution and role of time-dependent disturbances in the transition process of thermally driven boundary layers and in the complex interactions that lead to vortex breakdown deserves further attention. The appearance, and amplification and eventual breakdown of temporal wave-packet-like disturbances are the subject of a follow-on investigation. Time-modulated controlled spatial disturbances are introduced into the boundary layer and the evolution of the ensuing disturbances is reconstructed using surface liquid crystal sensors and particle image velocimetry (PIV) (Trautman 1999).

This work was supported by a National Science Foundation grant CST-9318332.

REFERENCES

Chen, C. C., Labhabi, A., Chang, H. C. & Kelly, R. E. 1991 Spanwise pairing of finite-amplitude longitudinal vortex rolls in inclined free-convection boundary layers. *J. Fluid Mech.* **231**, 73–111.

Farina, D. J., Hacker, J. M., Moffat, R. J. & Eaton, J. K. 1994 Illuminant invariant calibration of thermochromic liquid crystals. *Expl Thermal Fluid Sci.* **9**, 1–12.

Jaluria, Y. & Gebhart, B. 1973 An experimental study of nonlinear disturbance behaviour in natural convection. *J. Fluid Mech.* **61**, 337–365.

Jaluria, Y. & Gebhart, B. 1974 On transition mechanisms in vertical natural convection flow. *J. Fluid Mech.* **66**, 309–337.

Jeschke, P. & Beer, H. 2001 Longitudinal vortices in a laminar natural convection boundary-layer flow on an inclined flat plate and their influence on heat transfer. *J. Fluid Mech.* **432**, 313–339.

Joshi, S. S., Speyer, J. L. & Kim, J. 1997 A systems theory approach to the feedback stabilization of infinitesimal and finite-amplitude disturbances in plane Poiseuille flow. *J. Fluid Mech.* **332**, 157–184.

Klebanoff, P. S., Tidstrom, K. D. & Sargent, L. M. 1961 The three-dimensional nature of boundary-layer instability. *J. Fluid Mech.* **12**, 2–34.

Lloyd, J. R. & Sparrow, E. M. 1970 On the instability of natural convection flow on inclined plates. *J. Fluid Mech.* **42**, 465–470.

Schlichting, H. 1933 Zur entstehung de turbulenz bei der plattenstromung. *Nachr. Ges. Wiss. Göttingen*, 182–208.

Schubauer, G. B. & Skramstad, H. K. 1948 Laminar boundary layer oscillations on a flat plate. *NACA Rep.* 909.

Shaukatullah, H. & Gebhart, B. 1978 An experimental investigation of natural convection flow over and inclined surface. *Intl J. Heat Mass Transfer* **21**, 1481–1490.

Sparrow, E. M. & Husar, R. B. 1969 Longitudinal vortices in natural convection flow on inclined surfaces. *J. Fluid Mech.* **37**, 251–255.

Trautman, H. A. 1999 The manipulation of instabilities in a natural convection boundary layer along a heated, inclined plate. PhD Thesis, Georgia Institute of Technology.

Zuercher, E. J., Jacobs, J. W. & Chen, C. F. 1998 Experimental study of the stability of boundary-layer flow along a heated, inclined plate. *J. Fluid Mech.* **367**, 1–25.